GLOBAL MEAN SEA LEVEL HIGHER THAN PRESENT DURING THE HOLOCENE

Roger C. Creel*[1], Jacqueline Austermann[1], Robert E. Kopp[2], Nicole S. Khan[3], Torsten Albrecht[4], Jonathan Kingslake[1],

1. Lamont-Doherty Earth Observatory, Columbia University, New York, USA.
2. Department of Earth and Planetary Sciences and Rutgers Institute of Earth, Ocean, and Atmospheric Sciences, Rutgers University, New Jersey, USA.
3. Dept of Earth Science and Swire Institute of Marine Science, University of Hong Kong, Hong Kong.
4. Potsdam Institute for Climate Impact Research (PIK), Member of the Leibniz Association, Potsdam, Germany.

*rcreel@ldeo.columbia.edu

Abstract

Global mean sea-level (GMSL) change can provide insight on how ice sheets, glaciers, and oceans respond to warming[1;2]. The Holocene (11.7 ka to present) marks a time when temperatures may have exceeded early industrial (1850 CE) values[3]. Evidence from Greenland[4] and Antarctica[5;6] indicates that both ice sheets retreated inland of their present-day extents during the Holocene, yet previous GMSL reconstructions suggest that Holocene GMSL never surpassed early industrial levels[7–9]. We combine relative sea-level observations with glacial isostatic adjustment predictions from an ice-sheet model ensemble and new estimates of postglacial thermosteric sea-level and mountain glacier evolution to estimate Holocene GMSL and ice volume. We show it is likely (probability P=0.79) that GMSL exceeded early industrial levels in the mid-Holocene (8-4 ka) by up to 1.5 m and that the Antarctic Ice Sheet was likely (P=0.66) smaller than present in the last 6000 years. We demonstrate that Antarctic retreat lags Antarctic temperature by 250 years, underscoring future Antarctic vulnerability to present warming. Comparing our reconstruction to future projections indicates that GMSL rise in the next 125 years will very likely (P>0.9) be the fastest in the last 5000 years, and that by 2080 GMSL will more likely than not be the highest in 115,000 years.

The time interval extending from the start of the Holocene interglacial period (11.7 thousand years ago, ka) to the start of the industrial era (1850 CE, hereafter 'early industrial') marked the final melting of the two largest Northern Hemisphere ice sheets and the onset of a warm, stable interglacial. During this interval, polar temperatures may have temporarily exceeded early industrial temperatures by several degrees[10;11]. Studying global mean sea level (GMSL) during the Holocene, therefore, offers perspective on ice-sheet sensitivity to past and future warming.

Previous reconstructions of Holocene GMSL are mostly based on local relative sea level observations. Relative sea level (RSL) deviates from GMSL in part due to glacial isostatic adjustment (GIA), which describes the gravitational, rotational, and viscoelastic deformational effects of water and ice loading on the solid Earth[12]. GMSL studies therefore typically use GIA modeling to jointly refine ice-sheet reconstructions and solid Earth structure until the predicted RSL estimates fit observational constraints, then calculate GMSL from the reconstructed ice volumes[7–9;13]. For example, Peltier and colleagues iteratively modified a post-glacial ice reconstruction to fit geodetic uplift rates and RSL observations at a small set of far field sites and found that GMSL was less than a meter below present levels at 6 ka and gradually increased to reach present levels by 2 ka (extended Fig. 1, ref.[8]). Lambeck and colleagues, on the other hand, iteratively inverted far-field RSL observations for mantle viscosity and continental ice distributions to find that GMSL was more than 3±0.7 m below present at 6 ka and remained below present throughout the Holocene[7], a finding supported in a similar study by Bradley et al.[9]. None of these studies consider the possibility of an Antarctic Ice Sheet that was smaller in the Holocene than at early industrial.

In contrast to the models mentioned above, near-field evidence suggests that several sectors of the Antarctic

Ice Sheet retreated inland of their early industrial grounding lines before re-advancing during the mid-late Holocene[5;6;14]. This evidence includes sediment cores from ice-marginal lakes, sea-level indicators from raised beaches, radar observations of englacial structures, geodetic measurements of bedrock subsidence, and radiocarbon dates on sub-glacial organic carbon[15;16]. These polar constraints are supported by regional physics-based ice reconstructions that with a range of parameterizations reproduce Holocene readvance[17;18]. However, the field evidence and ice-sheet models do not uniquely constrain the timing and amount of retreat and readvance.

There are several reasons why previous studies could have mis-estimated Holocene Antarctic ice volume and GMSL. First, Holocene GMSL variation is expected to be much smaller than the LGM-to-present change, which is the main focus of the studies that produced these estimates (though not of Bradley et al.[9]). Second, these studies only had access to a fraction of the sea-level data now available, and did not include thermomechanical ice-sheet models coupled to oceanic/atmospheric forcing. Third, they do not account for lateral variations in Earth structure, an omission that could introduce biases[19]. Lastly, they underestimate uncertainties by providing single best estimates of GMSL or narrow confidence intervals. Lack of agreement in Holocene GMSL predictions led the International Panel on Climate Change Sixth Assessment Report (IPCC AR6) to assess, with medium confidence, a mid-Holocene (6 ka) GMSL 90% confidence interval of 3.5 m below present day to 0.5 m above present day, the spread of which is chiefly explained by the uncertain history of the Antarctic Ice Sheet during the Holocene[2].

To improve our understanding of Holocene GMSL and provide a far-field constraint on Holocene Antarctic Ice Sheet change, we pair a new postglacial (23 ka to 1850 CE) database of RSL observations with an ice-sheet ensemble via a novel algorithm that accounts for the influence of laterally varying Earth structure (see Methods for details). The database includes 10,253 sea-level data (Fig. 1) from low- to mid-latitude geological and biological archives such as salt marshes, mangrove swamps, coral reefs, and deltaic sediments[20]. The sea-level model 'prior' consists of a range of RSL predictions from an ice-sheet ensemble that combines several Northern Hemisphere simulations and 279 Antarctic simulations from the Parallel Ice Sheet Model (PISM), which span a mid-Holocene GMSL-equivalent range of $\sim$-16 to +2 m (Extended Fig. 2A)[17;21;22]. We include a large range of Antarctic histories in the ice-sheet ensemble because Holocene Antarctic variability is more uncertain than Greenland Ice Sheet behavior (Extended Fig. 3A)[15;23]. The model prior also includes novel probabilistic estimates of Holocene mountain glacier volume and thermosteric sea-level change. We use sea-level data and near-field observational constraints on the Antarctic Ice Sheet to calculate a posterior distribution of GMSL and Antarctic ice change. The efficacy of our approach is demonstrated with synthetic tests (see Methods and

Extended Fig. 4). In addition to inferring Holocene GMSL and Antarctic ice volumes, this approach allows us to compare the amplitude and rate of Holocene GMSL and Antarctic change to projected 21st century sea-level rise and Antarctic mass loss.

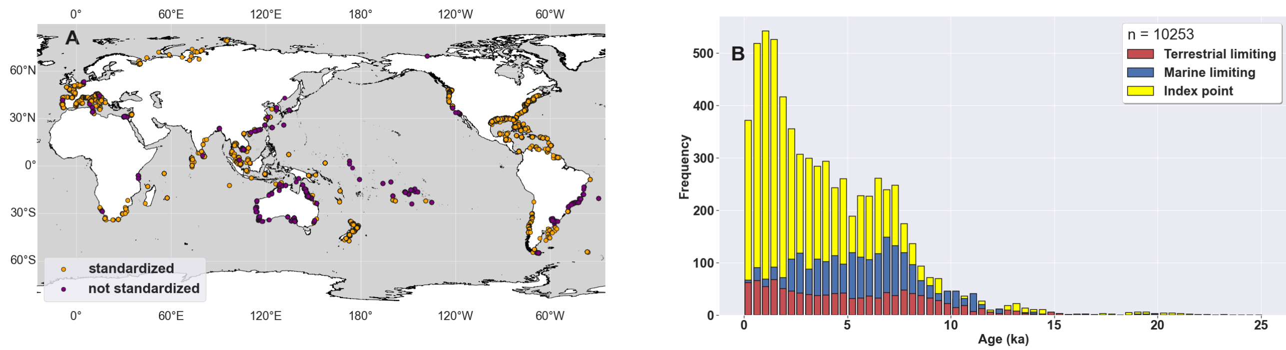

Figure 1: **(A)** Geographic distribution and **(B)** temporal frequency of relative sea level data. Orange markers in (A) denote data standardized following procedures agreed upon by the sea-level community (Table S1)[20]; purple markers denote additional data presented as originally published (Table S2). Red, yellow, and blue bars in (B) indicate, respectively, the number of terrestrial limiting data, index points, and marine limiting data. Bars plot on top of each other. Note that data below former ice sheets are not used in this analysis.

1 Holocene global sea level trends

The median of the final Holocene GMSL curve (hereafter the 'posterior') has three phases: rapid early-Holocene rise, slower mid-Holocene rise, then gradual late-Holocene fall (Fig. 2B). Rates of GMSL rise start to slow after 8 ka—a trend corresponding to the final Laurentide Ice Sheet termination (Extended Fig. 5A)[24]. The posterior reaches -0.9 m (-9.2 to 1.8 m, 90% credible interval) at 6 ka, which encompasses the IPCC-AR6 mid-Holocene GMSL estimate. This uncertainty range envelopes GMSL estimates from the ANU[7], ICE6G[8], PaleoMIST[13], and Bradley[9] ice models: PaleoMIST, Bradley, and ANU, which by 6 ka reach -6.6 m, -6 m, -2.9$\pm$0.7 m, respectively, fall below the posterior; ICE-6G, at -0.4 m by 6 ka, reaches above the posterior. The GMSL reconstruction likely (P=0.79) exceeds 0 m after 6 ka and peaks at 0.27 m (-3.1 to 1.0 m) at 3 ka (Fig. 2B inset). Evidence from RSL observations and Antarctic field constraints updates the prior to more strongly favor a GMSL peak of 0.5-1.5 m that occurs around 6 ka (Fig. 3C).

Our analysis reveals details of Antarctic ice volume that agree with recent field evidence but differ from previous GMSL studies. We find that the Antarctic Ice Sheet likely (P=0.66) shrank beyond its 1850 volume during the Holocene. The Antarctic Ice Sheet was likely smaller than present after 2.1 ka (0.1 to 8.0 ka) and reached a minimum of 0.1 m (-0.9 to 0.4 m) GMSL equivalent at 1.2 ka (Fig. 2C and inset). This timing aligns

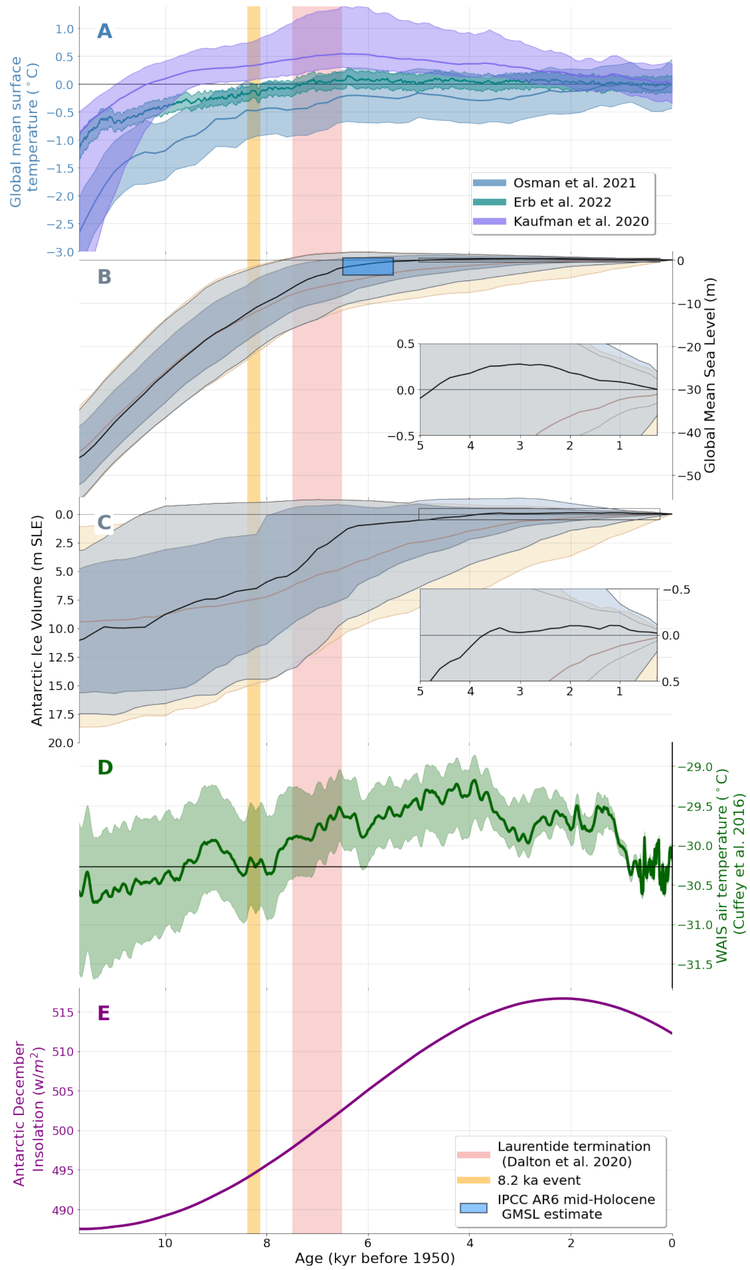

Figure 2: Holocene global mean sea level and Antarctic ice volume compared to climate variables. **(A)** Global mean surface temperature reconstructions[10;25;26]. **(B)** Global mean sea level. Brown and black lines denote the prior and posterior 50$^{\text{th}}$ quantile; tan and light gray bands the prior and posterior 90% credible intervals; and darker gray band the posterior 66% credible interval. Blue box demarcates the IPCC AR6 mid-Holocene global mean sea level estimate. **(C)** Antarctic ice volume. **(D)** Air temperature from the West Antarctic Ice Sheet Divide core[11]. Green envelope in D is 95% confidence interval. Black reference line denotes temperature mean over the last millennium. **(E)** Antarctic December insolation. Pink and orange vertical lines indicate final Laurentide termination[24] and the 8.2 ka event, respectively.

with geomorphological, sedimentary, and geophysical evidence from Antarctica[15]. We find that Antarctic ice volume closely tracked both insolation and West Antarctic terrestrial temperature (Fig. 2C, D, E). The posterior median Antarctic ice volume estimates are smaller than the prior median Antarctic distribution for virtually the entire Holocene, during some intervals by up to 4 m GMSL equivalent (Fig. 2C). Further, evidence from sea-level data and nearfield constraints heavily favors an Antarctic Ice Sheet that shrinks to ∼0.5-1.5 m smaller than its present volume between 8 and 4 ka (Fig. 3D, E, F). Since differences between posterior and prior distributions indicate that the data constraints have added information to the model, this result demonstrates that intermediate- to far-field RSL data can help distinguish detailed variations in Holocene Antarctic ice volume.

Postglacial RSL data and near-field Antarctic constraints are not able in this modeling framework to differentiate between the other sea-level contributors, including Northern Hemisphere ice sheets, mountain glacier histories, and thermosteric effects; the posterior distributions of these contributors therefore does not change relative to the prior. This is likely because of the small amount (< 0.2 m) that thermosteric effects (extended Fig. 6) and mountain glacier histories (extended Fig. 7A) likely contributed in the last 6000 years as well as the smaller number of Northern Hemisphere ice-sheet simulations included in our model relative to the number of Antarctic simulations.

2 Antarctic Ice Sheet driven by local temperature

Recent debate surrounding future Antarctic Ice Sheet instability has focused attention on the processes responsible for Antarctic Ice Sheet behavior during the Holocene. Antarctic ice volume may have followed polar temperature[27], as likely happened in Greenland[28]. Alternatively, Antarctic readvance may have been driven by GIA, because isostatic rebound in areas of ice-sheet retreat can reground ice sheets[5;14;29]. While our model does not provide causal evidence to distinguish between these hypotheses, we find a significant cross correlation (∼0.5) between Antarctic ice volumes, austral summer insolation, and local temperature records. Late-Holocene Antarctic volume minima at ∼3.6, 2.0, and 1.0 ka lag West Antarctic temperature maxima at 3.9, 2.2, and 1.3 ka by 250 years and broadly align with the local insolation maximum at 3-1.5 ka. This correspondence points to temperature forcing as a likely driving mechanism (Fig. 2C, D, E). Antarctic marine temperature records indicate that polar waters reached their warmest at ∼6 ka[10], and terrestrial sedimentary records[30] and isotopic evidence from the West Antarctic Divide ice core[11](WDC) support a climatic optimum between 6 and 3 ka (Fig. 2D). Although WDC surface air temperatures were used to force the PISM Antarctic Ice Sheet models,

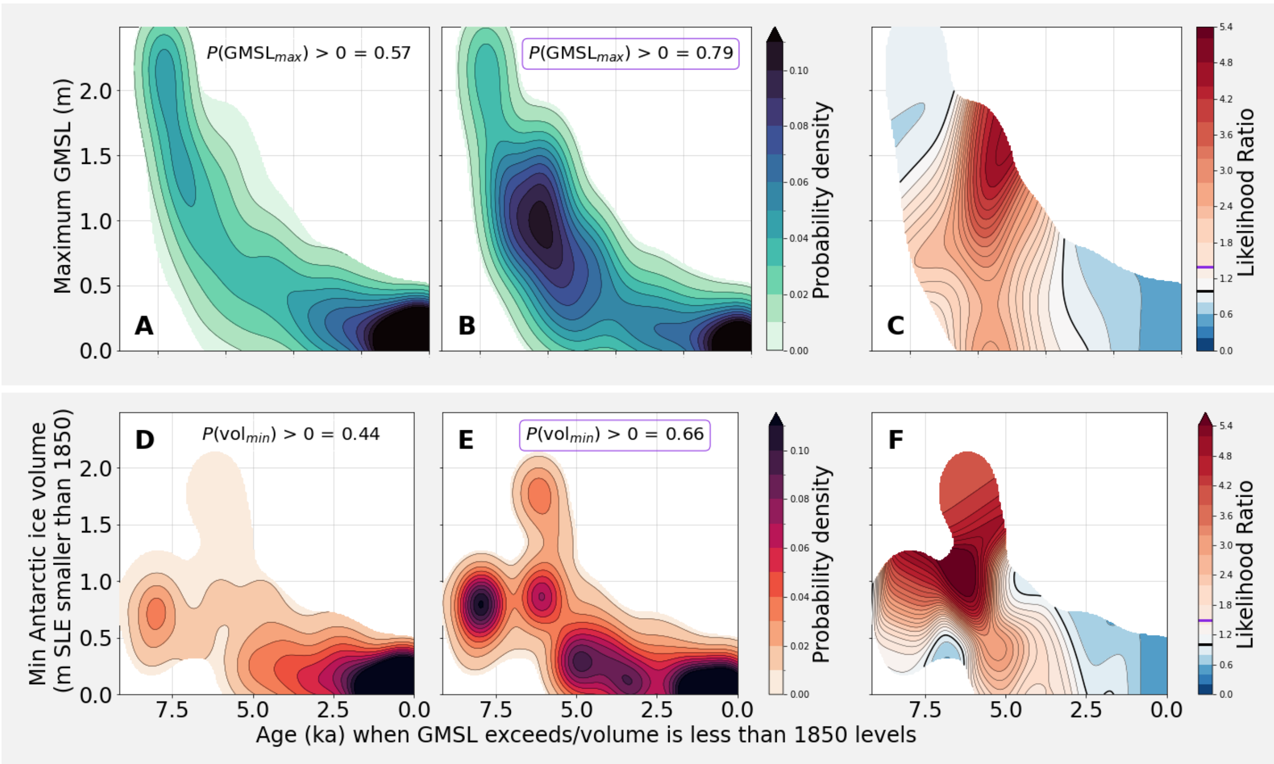

Figure 3: Maximum amplitude and time of pre-industrial exceedance of global mean sea level and Antarctic ice volume minimum for global ice-sheet scenarios. Top row **(A)**: Prior probability distribution of model maxima and time each model first exceeds present levels, i.e. distribution without weighting by RSL observations and Antarctic constraints. **(B)** Posterior distribution of (A). $P(GMSL)_{max}$ denotes that probability that prior (A) or posterior (B) GMSL exceeded present levels. **(C)** Likelihood ratio, calculated as the ratio of (B) to (A), which represents the degree to which the data constraints have increased the likelihood of a given maximum GMSL. Bottom row **(D/E/F)**: Prior distribution, posterior distribution, and likelihood ratio for Antarctic ice volumes. $P(vol)_{min}$ denotes that probability that prior (C) or posterior (D) Antarctic Ice Sheet volume was smaller than at present. Black line on colorbars for (C) and (F) denotes a likelihood ratio of 1, which indicates no increase in likelihood; Purple line on colorbars denotes the likelihood ratio of the probability that GMSL exceeded present levels or the Antarctic Ice Sheet was smaller than today; values higher than one indicate that exceedence or smaller-than-present volume are more likely in the posterior than the prior. Ice volumes are shown in GMSL equivalent units.

a smaller-than-present Antarctic Ice Sheet before 3 ka is not favored in our prior, as one would expect given the generally higher WDC temperatures prior to 3ka (Fig. 3D). Nevertheless, the posterior distributions place considerable probability density on GMSL higher and Antarctica smaller than present levels prior to 3 ka and as early as 7-5 ka (Fig. 3C). This lends credence to arguments that summer insolation, local temperatures, and Antarctic Ice Sheet variations are tightly coupled[31;32]. These links do not preclude other explanations for Antarctic readvance such as isostatic uplift, but rather motivate further work to understand the timing of GIA-driven rebound and its potential role in Holocene Antarctic ice dynamics.

3 Perspective on interglacial temperature

Our findings suggest that GMSL and global temperature are decoupled during the Holocene. Estimates of Holocene global mean temperatures, generated from diverse combinations of sea surface temperature proxies, terrestrial temperature data, and climate model outputs, vary from monotonic temperature increase[26;33] to a mid-Holocene temperature peak of between 0.1°C[25]and more than 0.4°C[10;34](Fig. 2A). These temperature histories differ from our GMSL reconstruction, which most likely exceeded present level but only reached its maximum in the late Holocene (Fig. 2B). While it is expected that GMSL would lag temperatures, it is important to consider that global mean temperature integrates insolation variation across all latitudes, while GMSL is driven principally by polar ice mass changes, which can lag decades (mountain glaciers[35]), centuries (Greenland Ice Sheet[4]), or millennia (Laurentide Ice Sheet[36]) behind high-latitude temperatures. Efforts to understand our GMSL commitment for each degree of warming regularly use past periods when global mean surface temperature and GMSL were higher than today as analogues for a future warming world[37;38]. Our results indicate that this approach could be improved by instead targeting high-latitude temperature records that characterize the behavior of individual ice sheets. This distinction is particularly important when high-latitude temperatures are out of sync between the northern and southern hemisphere, as likely occurred during the Last Interglacial[39].

4 Contextualizing modern sea level rise

A central role of paleoclimate research is to place anthropogenic climate change in the context of natural climate variability. Here, we do this by comparing our peak Holocene GMSL estimates to future sea-level projections from the International Panel on Climate Change's Sixth Assessment Report[2]. Rates of future GMSL change between 2005 and 2150 will very likely (P>90%) be the highest in the last 5000 years and more likely than not (P>50%) the highest since the Laurentide Ice Sheet collapsed at around 7 ka (Fig. 4B). The rate of GMSL rise over the historical period (1850 to 2005) is likely (P>65%) higher than rates over the last 5000 years but very unlikely (P<10%) higher than over the last 7000 years. Future GMSL will more likely than not (P>50%) exceed maximum Holocene GMSL by 2080 under all emissions scenarios (Fig. 4A). By 2150, future GMSL will likely (P>64%) be higher than peak Holocene GMSL under low emissions (SSP1-2.6) and very likely (P >90%) higher under high emissions (SSP5-8.5) (see Methods).

By contrast, rates of Antarctic Ice Sheet volume loss during the historical period are very unlikely (P<0.1) to be higher than in the past 4000 years. In the future, it is more likely as not (P >0.5) that rates of Antarctic Ice Sheet shrinkage will be higher than the last 4000 years, but unlikely that they will be higher than during the last 7000 years (Fig. 4D). However, rates of GMSL rise under the highest emissions scenario (SSP5-8.5, low-confidence), which hinges on poorly understood Antarctic Ice Sheet processes, may exceed any Holocene rates (Fig. 4B). And because of the lag between temperature and ice-sheet mass loss, should high emissions continue beyond the 21st century, GMSL would likely continue to rise faster than any Holocene rates for several hundred years, only slowing after the complete collapse of the West Antarctic Ice Sheet[40]. Our results therefore add urgency to the need for a better understanding of Antarctic Ice Sheet dynamics during the present interglacial, the mechanisms that drive these dynamics, and the implications for future Antarctic ice stability.

Earth's climate in the past 9000 years has been unusually stable relative to past environmental changes. This 'safe operating space'[41] enabled the rise of agriculture, civilization, and industrialization. Our results indicate that projected future rates of GMSL rise exceed rates for the past 7000 years but are comparable to those that early Holocene civilizations experienced. However, this equivalence belies the vast differences between how modern and ancient human societies adapted to sea-level rise. Humankind prior to 8 ka consisted of fewer than 50 million people, many of whom were migratory[42]. Modern human civilization in the 21st century is projected to near 10 billion people[43], hundreds of millions of whom live in permanent coastal communities that cannot be relocated inland. The 'safe operating space' for sea-level rise will be smaller for future generations than it was for past cultures.

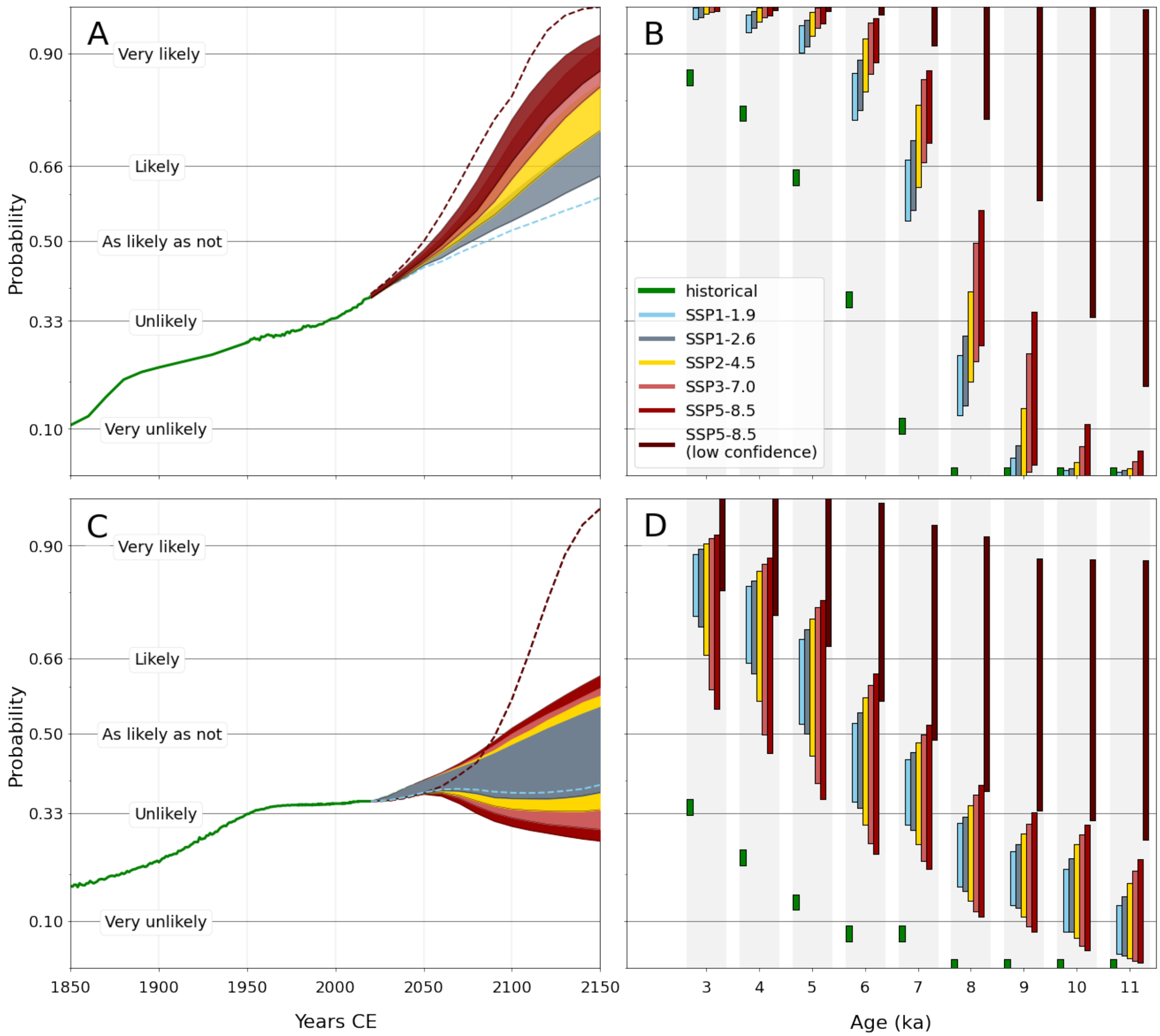

Figure 4: Probability over the period between 1850 and 2150 that GMSL and Antarctic Ice Sheet volume change and rates of change exceed Holocene levels and rates of change. **(A/C)** Probability that the level of GMSL (A) or Antarctic ice volume (C) exceeds the maximum Holocene (11.7 ka to 1850 CE) level. **(B/D)** Probability that the rate of historic (1850 to 2005) or future (2005 - 2150) change of GMSL (B) or Antarctic ice volume (D) is greater than the maximum rate of change over the last 3, 4, 5, 6, 7, 8, 9, 10, or 11 kyr. Green lines between 1850 to 1950 (A) or 1979 (B) represent probabilities from calculated relative to GMSL values from (ref.[44]) and (ref.[45], see Methods), respectively. Green lines between 1950 (A) or 1980 (B) and 2020 represent exceedence probabilities calculated relative to observed GMSL or Antarctic ice volume as reported by IPCC AR6[2]. Solid color bands in (A/C) represent future exceedance probabilities from 2020 to 2150 calculated relative to likely ranges for SSP1-2.6 through SSP5-8.5 for processes in which there is at least medium confidence, as assessed by IPCC AR6. Dashed sky blue and dark red lines in (A/C) respectively represent the lower end of the likely range for SSP1-1.9 and the upper 83^{rd} percentile of low-confidence projections for SSP5-8.5. Green bars in (B/D) represent the probabilities that the average rate of historical sea level rise (1850 - 2005) exceeds the maximum rate of Holocene sea level rise during the last 3 to 8 kyr, as noted in vertical grey bars.

165 # Extended Figures

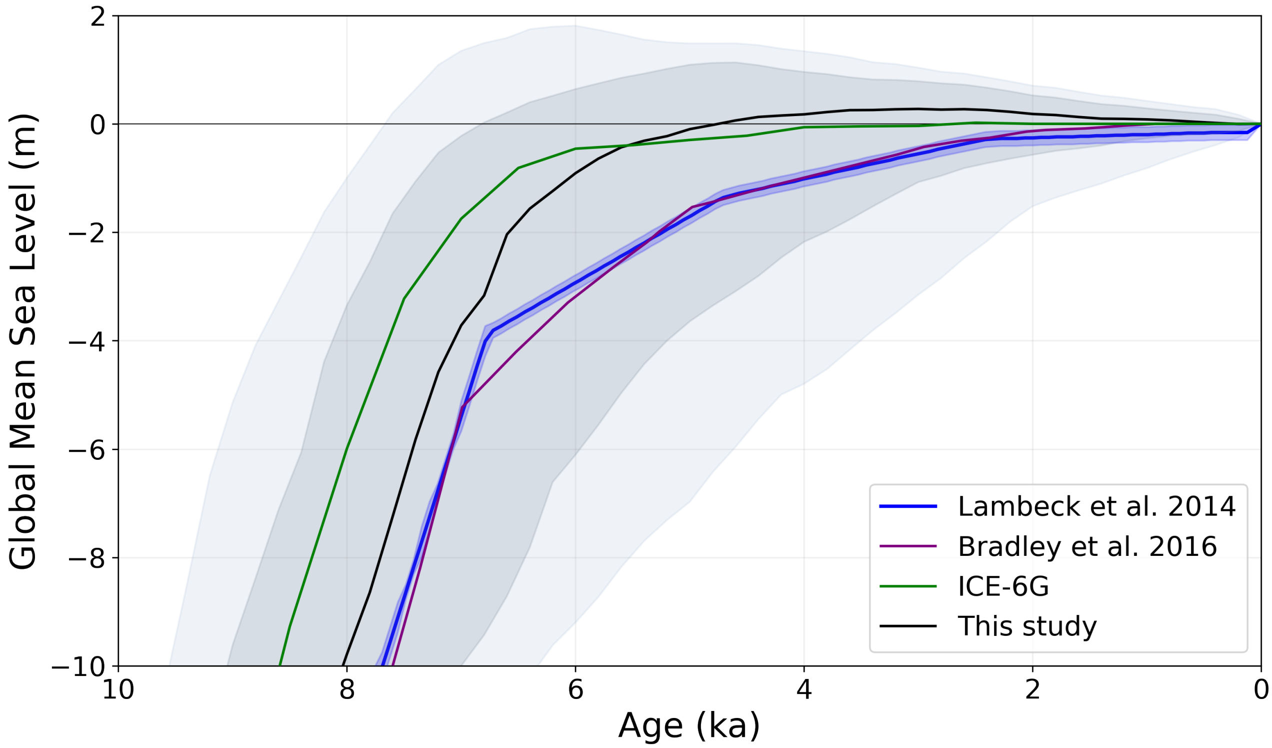

Extended Figure 1: Global mean sea level 10 ka - present. Green line and Blue line with 95% credible interval are ice volume equivalent sea level from ICE-6G_C (VM5a)[8] and Lambeck and colleagues[7]. Purple line is ice-volume equivalent sea level from Bradley and colleagues[9], which is corrected for ice above floatation. Black line with 66% (darker grey) and 90% (lighter grey) credible interval is this study.

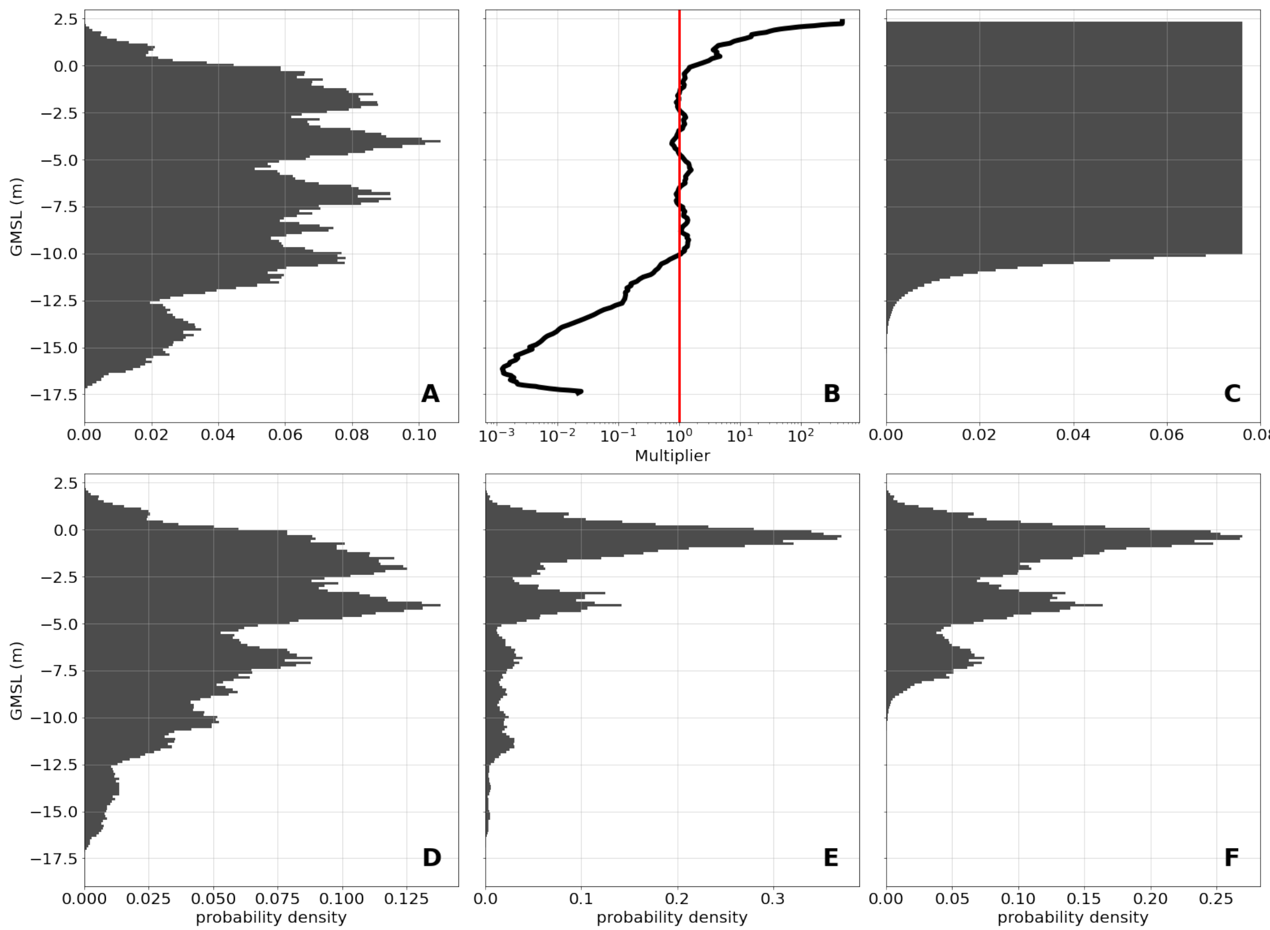

Extended Figure 2: Modeled distributions of global mean sea level (GMSL) in the mid-Holocene (6 ka) demonstrating how data-derived weights are combined to generate the posterior. **(A)** Prior GMSL distribution with each ice-sheet model assigned equal weight. **(B)** Correction factor applied to GMSL curves so that they have even probability density between -10 and +2 m. Red line denotes a correction factor of one, i.e. no correction applied. Note that a log scale is used on the x axis. **(C)** Corrected prior GMSL distribution. **(D)** Posterior GMSL distribution using only weights derived from RSL data. **(E)** GMSL curves weighted only by Antarctic Ice Sheet (AIS) fitness scores from[17;21;22]. **(F)** Posterior model distribution produced by applying RSL weights and AIS fitness scores to the uniform prior GMSL distribution.

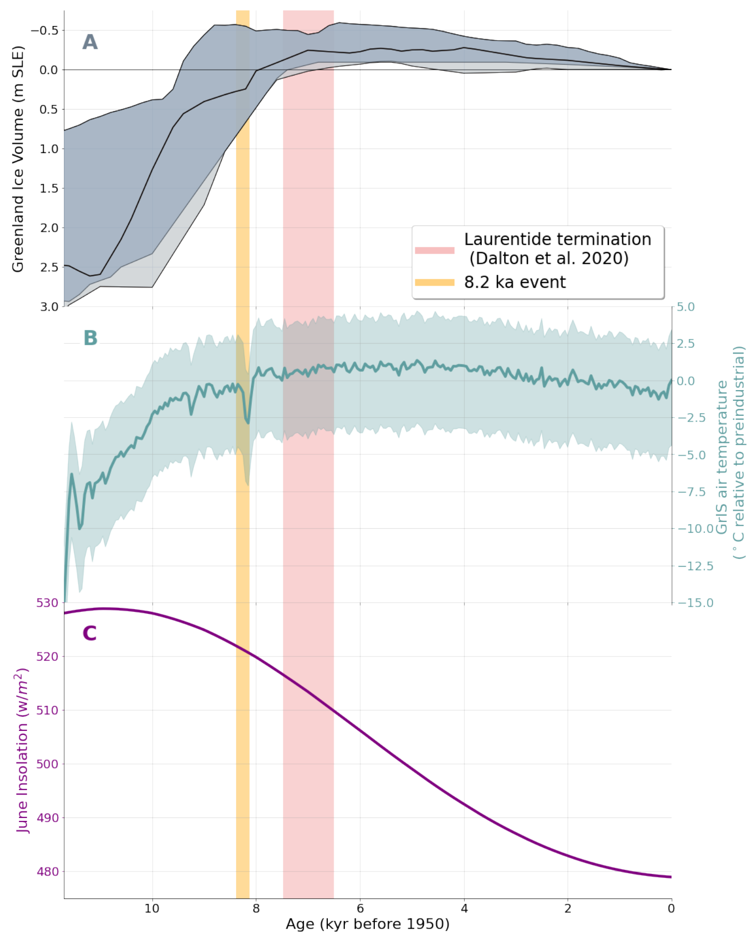

Extended Figure 3: Holocene Greenland ice volume compared to climate variables. **(A)** Greenland ice volume. Black line denotes posterior 50$^{\text{th}}$ quantile; light gray band the posterior 95% credible interval; and darker gray band the posterior 66% credible interval. Prior mean and credible intervals (not shown) are identical to the posterior. (B) Greenland Ice Sheet surface air temperature data assimilation product[46]. Green envelope is 95% confidence interval. Green line denotes mean. (C) June insolation at 65° North. Pink and orange vertical lines indicate final Laurentide termination[24] and the 8.2 ka event, respectively.

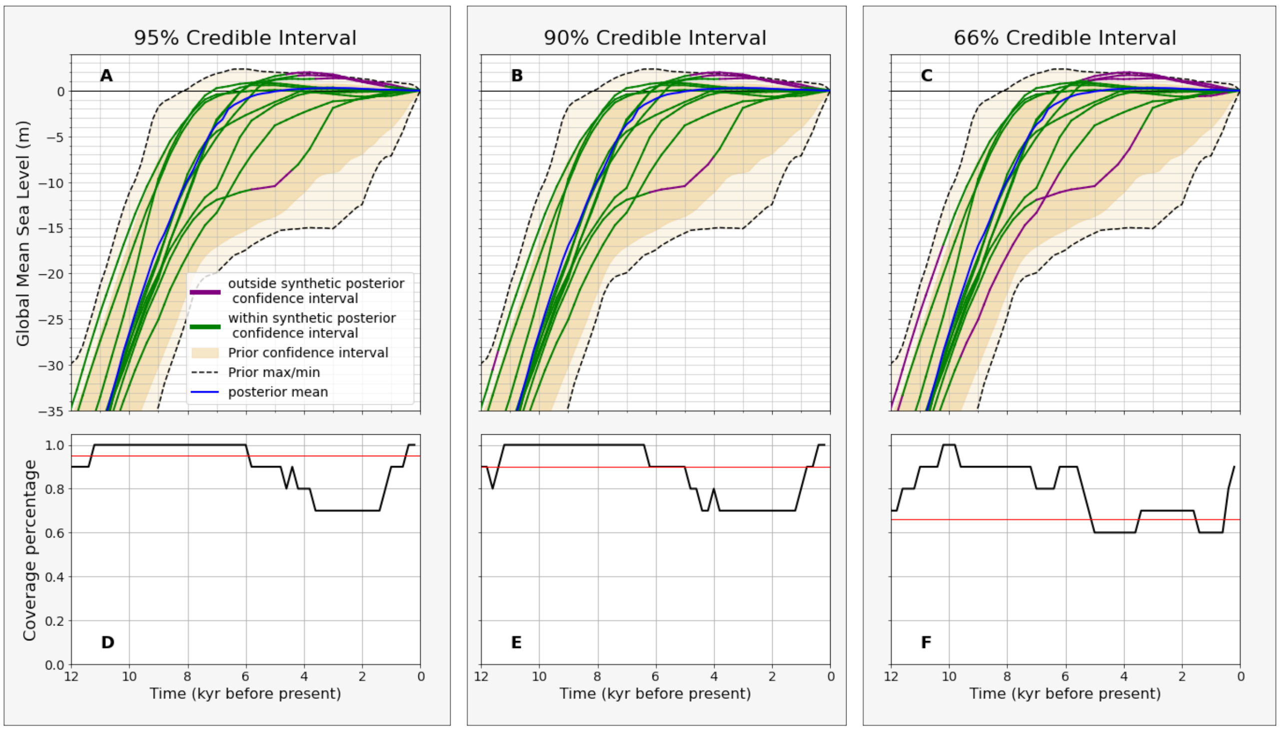

Extended Figure 4: Results of synthetic tests of data assimilation algorithm. **(A)** Tan envelope denotes 95% credible interval of prior global mean sea level (GMSL) ensemble. Green/purple Lines trace the 'true' GMSL curves used to generate synthetic relative sea level data, with color denoting time steps where the 'true' GMSL curve is (green) or is not (purple) within the credible interval of the posterior GMSL curve (see methods). Blue line is the posterior mean curve from Fig. 2. **(B-C)** Identical to (A) but with, respectively, a 90% and 66% credible interval. **(D-F)** Coverage percentage, i.e. percentage of posterior models in (A-C) whose credible interval successfully captures the associated 'true' synthetic GMSL curve. Red line indicates approximate percentage cutoff considered successful for each interval, e.g. 95% of 'true' curves should fall within the 95% credible interval of the synthetic posterior.

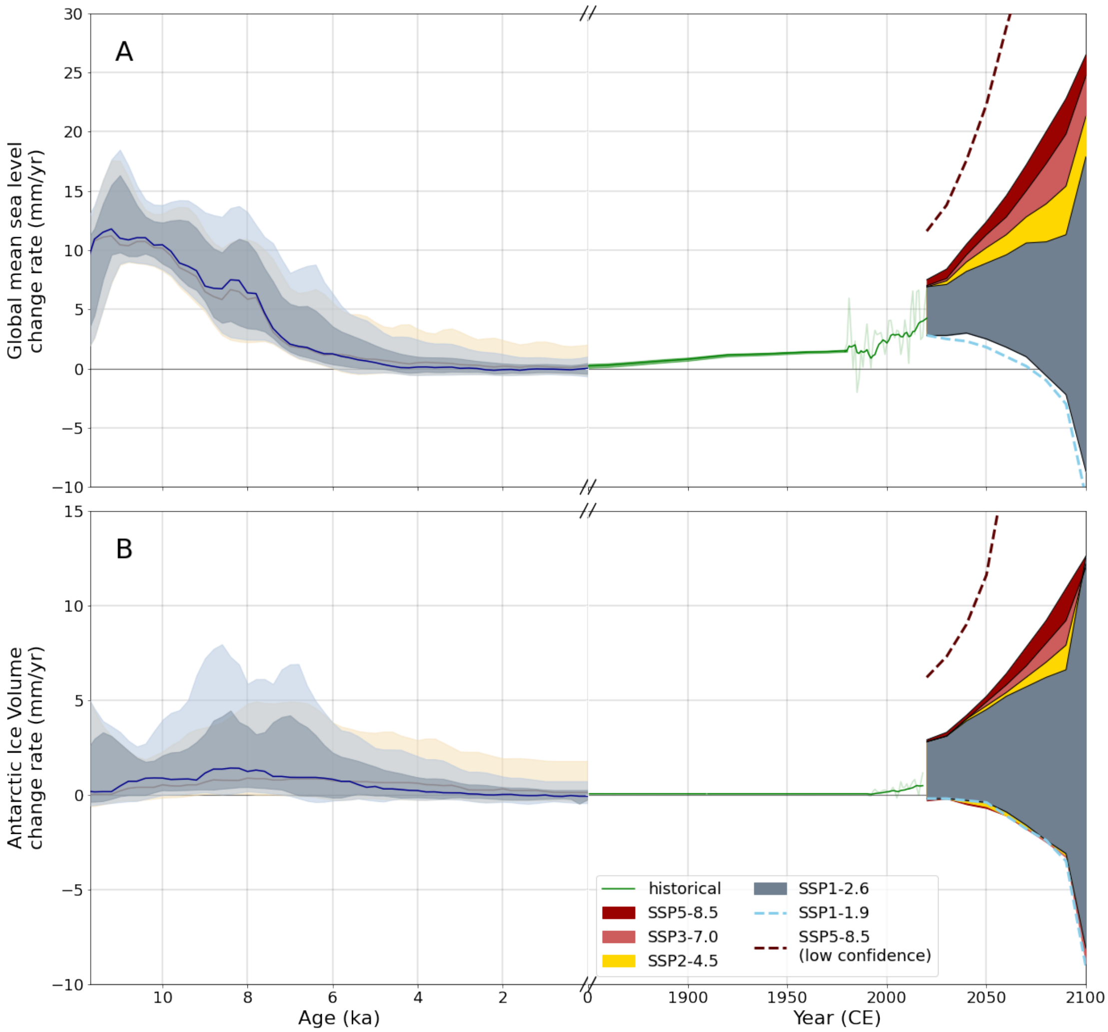

Extended Figure 5: Rates of global mean sea level and Antarctic ice volume change 12 ka - 2100 CE. **(A)** Rates of global mean sea level change. **(B)** Rates of Antarctic Ice Sheet volume change. Rates prior to 1850 are from this study. Historical rates 1850 to 1950 are from ref.[44] (A) and ref.[45] (B). Rates 1950 to 2100 are from the IPCC AR6[2]. See Figs. 2 and 4 for further details.

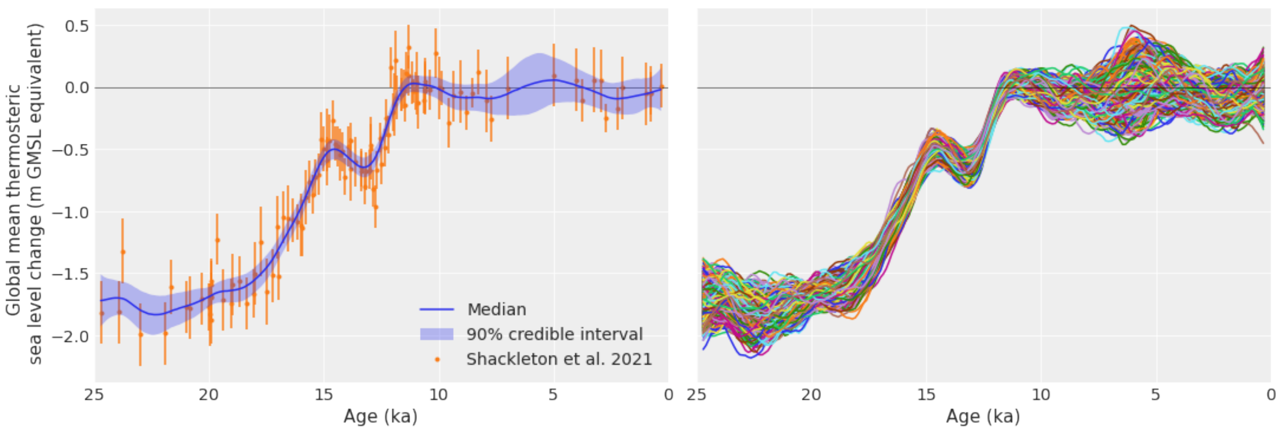

Extended Figure 6: Thermosteric sea-level change 25 ka - present in meters global mean sea level (GMSL) equivalent. Orange markers denote thermosteric sea-level estimates derived from[47]. Blue envelope indicates 90% credible interval derived from Gaussian process regression fit to empirical estimates. Colored lines are random draws from posterior distribution.

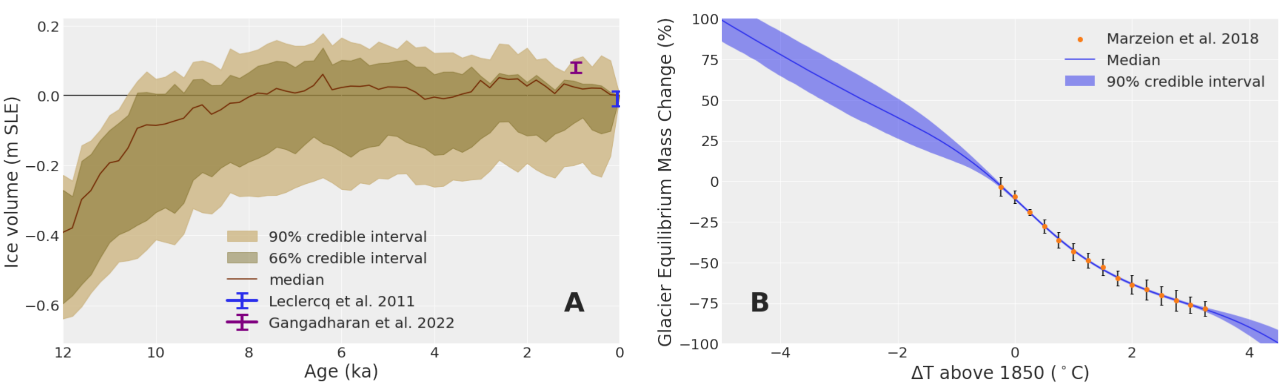

Extended Figure 7: **(A)** Mountain glacier posterior volume in global mean sea level-equivalent units. Light bown indicates 90% credible interval; darker brown denotes 66% credible interval. Prior volume, not shown, is identical to posterior volume. Purple and blue error bars denote empirical estimates of the mountain glacier contribution to global mean sea level from ref.[48] and ref.[49], respectively. **(B)** Mountain glacier equilibrium mass change per degree of temperature change relative to 1850. Orange dots denote empirical mass change - temperature scaling relations[50]. Blue envelope indicates 90% credible interval from Gaussian process regression fit to extended empirical estimates.

METHODS

Sea level data

Sea-level observations are taken from two sources: HOLSEA-standardized papers (n=7923, Table S1), hereafter called HOLSEA data[20], and published sources not yet compiled into HOLSEA format, hereafter called non-HOLSEA data (n=2330, Table S2). To be included, non-HOLSEA sea-level observations must have locations specified to within 2 km; age in calendar years before present; measured or reasonably estimated elevation; and indicative meaning composed of reference water level and indicative range, which respectively define where the indicator formed relative to tidal levels and the 95% confidence range that the indicator occupied[51]. Beyond these criteria, standardized data have an array of additional metadata, including comprehensive estimation of and justification for elevation, age, and inferential uncertainties[20]. Preference in selecting non-HOLSEA papers was given to regions not represented in the HOLSEA database and to data calibrated with IntCal20/Marine20/ShCal20[52–54]; no data was recalibrated for this study. RSL observations from Greenland, Canada, Northern New England, Fennoscandia, British Isles, and Antarctica are excluded from this analysis because of their sensitivity to local mantle viscosity, which limits their utility for GMSL and ice volume inference. RSL observations are distributed globally, with the highest data density in Europe, the US, Australia, and Southeast Asia, and data gaps along the West African coastline and in Alaska, Siberia, Northwestern South America, and the Middle East (Fig. 1). RSL data range in age from 24,295 ka to 1850 CE, and consist of 6664 index points and 3589 limiting points.

Constructing the Glacial Isostatic Adjustment ensemble

The sea-level observational dataset assembled for this study is compared to spatiotemporal RSL fields produced by combining estimates of barystatic and thermosteric sea-level change. Predictions of barystatic sea level (h_b), defined as the changing proportion of water stored on land and in the ocean[55], are produced by an ensemble of GIA models. Thermosteric sea-level change (h_θ), defined as the temperature-driven expansion or contraction of the global ocean volume divided by the ocean surface area[55], is derived from proxy reconstructions of global mean ocean temperature[47].

The GIA models follow a gravitationally self-consistent sea-level formulation that accounts for the migration of shorelines and feedbacks into Earth's rotation axis[56;57]. For the ensemble, we pair various ice thickness histories with a suite of Earth structures. We assume that the elastic structure of Earth's interior follows

PREM (Preliminary Reference Earth Model)[58]. For the viscous structure, we vary the elastic thickness of the lithosphere (71 and 96 km), upper mantle viscosity (2, 3, 4, and 5 x 10^{20} Pa S), and lower mantle viscosity (3, 5, 7, 8, 9, 10, 15, 20, 30, 40, and 50 x 10^{21} Pa s). These parameters accord with the range of viable solid Earth structures found by previous RSL data-GIA model comparisons to fit the mid- to low-latitude regions considered here[7;9].

Global ice-sheet reconstructions are constructed by assembling all combinations of 4 Laurentide, 4 Eurasian, 6 Greenland, 1 Patagonian, and 279 Antarctic Ice Sheet histories, then pairing each combination with one of 200 mountain glacier scenarios. Northern Hemisphere ice-sheet reconstructions used include the ANU[59–61], ICE-6G[8], GLAC1D[62;63], and PaleoMIST[13] models. The Huy3[64] and VAR[65] models are included as additional Greenland Ice Sheet reconstructions because of their modest minimum mid-Holocene volume. The Patagonian Ice Sheet history from PaleoMIST is included in all models.

Antarctic ice histories used include 256 Parallel Ice Sheet Model (PISM) ensemble members from Albrecht et al.[17] and an additional 23 histories from Albrecht et al.[22] chosen because they reach a volume smaller than present during the Holocene. All of the ice histories used here already include a glacial phase (commencing at 80 ka or earlier) except for ICE-6G, the GLAC-1D Eurasian Ice Sheet, the ANU Laurentide Ice Sheet, and the VAR Greenland Ice Sheet. For ICE-6G, a global glaciation phase between MIS-5a (80 ka) and the Last Glacial Maximum (LGM, 26 ka) is constructed to match a GMSL curve based on RSL observations and δ^{18}O records from benthic foraminifera[66]. Glacial ice configurations are assumed to be identical to postglacial geometries with the same GMSL value. Next, ice volumes are calculated for the pre-LGM ICE-6G Eurasian, Laurentide, & Greenland Ice Sheets. These Eurasian, Laurentide, and Greenland Ice Sheet volume histories are then used to construct pre-LGM GLAC-1D, ANU, and VAR ice-sheet histories by matching the glacial histories to post-LGM GLAC-1D, ANU, and VAR ice-sheet configurations with the same volume. All GIA simulations are run from 80 ka to present.

Mountain glacier ice volumes are reconstructed for the past 80 ka. Spatiotemporal estimates of temperature anomalies from 24 ka to present relative to 1850 are taken from the Holocene DA[25] and LGMR[26] reanalysis products. A 200-member paleotemperature ensemble is constructed by pairing 100 random samples from the Holocene DA (0-12 ka) with 100 samples from the LGMR (12-24 ka), then combining those 100 postglacial temperature histories with an additional 100 random samples from the LGMR ensemble (0-24 ka). Temperature ensemble members are linearly interpolated to a degree 256 Gauss Legendre grid. An existing scaling relation of the equilibrium mountain glacier volume response to global mean temperature changes[50] is expanded to cover

-5 to +4.5 $^{\circ}C$ using Gaussian process regression with a Matérn 3/2 kernel and a linear prior (see extended fig. 7). This scaling relation is mapped onto the paleo-temperature ensemble to create a spatiotemporal mountain glacier scaling field. Early industrial mountain glacier mass and area estimates (1901)[67] are converted to volume assuming an ice density of 920 kg m^{-3}, then multiplied by the scaling field to produce a time- and space-varying ensemble of mountain glacier volumes 24 - 0 ka. Glacier volumes are assumed to linearly increase between 80 and 24 ka. Though this assumption elides the details of mountain glacier volumes prior to LGM, the volumes are so small that this choice should not affect the Holocene GMSL inference. A random sample from the mountain glacier ensemble is added to each ice history.

The mountain glacier ensemble produced here accords within uncertainties with quantitative estimates of Holocene mountain glacier contribution to Common Era sea level, which suggest -0.9$\pm$2.1 cm of glacier contribution to GMSL from 1800 to 1850[49] and a maximum of 8$\pm$1.5 cm of glacier contribution at $\sim$900 CE relative to 1850 CE[48]. It also agrees with more qualitative assessments of minimal mountain glacier volumes in the early-mid Holocene followed by a readvance to the Little Ice Age maximum[35;68]. The procedure outlined above assumes that Holocene mountain glaciers are in equilibrium with local temperature. While the mountain glacier response to changing climate depends on glacial geometry and local climate conditions, glacial volume in most regions lags glacier length by 30 to $\sim$200 years[69] and glacier length in turn lags temperature by 50-200 years[70]. These lags are similar in magnitude to the 200 temporal resolution of our model and are based on measurements from a small fraction of all mountain glaciers[69]. Our assumption of mountain glaciers being in equilibrium with temperature is therefore likely a simplification but one that appears appropriate given the temporal resolution of this study.

Combining all reconstructions yields 26,784 ice-sheet histories (ice-sheet ensemble), which, when paired with the 88 different Earth structures, results in 2,356,992 RSL fields (GIA ensemble). All ice models are linearly interpolated onto a Gauss Legendre grid of degree 256, which represents a spatial resolution of $\sim$1 degree. GIA calculations are performed at this resolution. Ice volume changes used for the GMSL reconstruction are defined as exclusively ice above floatation following ref.[71] sections 2 and 4; Antarctic ice volume changes are defined as inclusive of ice above and below floatation.

Thermosteric sea-level change is derived from a mean ocean temperature reconstruction 25—0 ka[47] using a linearized equation of state[72]:

$$h_\theta = \alpha \Delta T h_o \tag{1}$$

where α, the thermal expansion coefficient, is 1.7 x 10^{-4}; h_o, the average depth of the ocean, is 3688 meters; ΔT is the change in mean ocean temperature; and h_θ is ocean thermal expansion. The thermosteric sea-level estimates were modeled using a Gaussian process regression with a Matérn 3/2 kernel (see Extended Fig. 6). Thermosteric sea level during the Holocene reaches a maximum median value of 0.05 (-0.13, 0.26, 90% credible interval) m above present at 5 ka and remains within 10 cm of present values throughout the Holocene. Using a higher-order Taylor expansion[73] yielded results that differed by less than 1 mm over the Holocene and between 1 and 20 mm during the deglaciation. Random samples drawn from the thermosteric posterior were then added as a spatially uniform, time-varying field to the GIA ensemble before these fields were compared to sea level data (Extended Fig. 6B). The inclusion of thermosteric effects, as well as of mountain glaciers, was found to have a minimal effect on the posterior. This suggests that the model is not sensitive to factors such as thermal expansion and glacier volumes that likely dominated centennial-scale GMSL variability over the last few thousand years.

Data assimilation algorithm

We estimate Holocene GMSL by conditioning the GIA ensemble on the RSL database to derive a probabilistic posterior. Data assimilation is performed on 1) the entire dataset, 2) a dataset that includes only the HOLSEA standardized data, and 3) a synthetic dataset (see section 4). Because each of these data (sub)sets are analyzed in the same way, this section will for simplicity refer to a singular 'RSL database' in order to describe the algorithmic design.

We group observations from the RSL database by geographic location, using a site size of 5 degrees lat / lon (see Fig. 1 for data locations and Fig. 5A for sites). Grouping is performed to account for geographic clustering of data; each site receives equal weight in the following misfit analysis. Varying site size by two degrees was found to change the posterior GMSL median <0.02 m over the last 6 kyr, <1 m between 6 and 8 ka, and 1-4 m between 8 and 11.7 ka, and the posterior Antarctic Ice Sheet median by <0.02 m over the last 7 kyr and <0.3 m between 7 and 11.7 ka—differences that are much smaller than the posterior uncertainty. Repeating our analysis with only HOLSEA-standardized data was found to increase the posterior GMSL(Antarctic Ice Sheet) median by <0.01(<0.02) m over the last 6 kyr and an average of 0.4(0.15) m between 6.5 and 12 ka.

A fitness score is derived for each sea-level index and limiting point by comparing them to a member of the GIA ensemble via a weighted residual sum of squares (WRSS) calculation following Creel et al.[74] and similar to Briggs and Tarasov[75], which accounts for elevation and age uncertainties in both index and limiting points:

$$\mathcal{W}_{nm} = \begin{cases} \left(\frac{2r^t_{nm}}{\varepsilon^t_n}\right)^2 + \left(\frac{2r^y_{nm}}{\varepsilon^y_n}\right)^2 & c_n = 0 \\ \left(\frac{2r^t_{nm}}{\varepsilon^t_n}\right)^2 - 2\, ln\left(\frac{1}{2} + \, \frac{1}{2} erf\left(c\frac{r^y_{nm}}{\epsilon^y_n}\right)\right) & c_n \neq 0 \end{cases} \tag{2}$$

$\mathcal{W}_{nm}$ is the WRSS for datapoint n and GIA ensemble member m, r^y_{nm} and r^t_{nm} are the residuals in sea level and time, respectively, between datapoint n and GIA ensemble member m, and ϵ^y_n and ϵ^t_n are the data uncertainties (assumed to be independent and normally-distributed) in sea level and time, respectively. Further, $c = 0$ when the observation is a sea level index point, $c = -1$ if the datapoint is marine limiting and $c = 1$ if the datapoint is terrestrial limiting. A chi-squared value, χ^2_{ms}, is calculated by taking the mean of WRSS scores for each GIA ensemble member m at each site s:

$$\chi^2_{ms} = \frac{\sum_{n=1}^{N} (\mathcal{W}_{nm} \cdot \delta_{ns})}{\sum_{n=1}^{N} \delta_{ns}} \tag{3}$$

where N is the number of observations in the RSL database. $\delta_{ns} = 1$ if datapoint n is in site s, otherwise $\delta_{ns} = 0$. For the next step we consider that each GIA ensemble member m can be described by a combination of ice model i and Earth structure e, i.e. χ^2_{ms} can be written as χ^2_{ies}. We next calculate the best possible misfit value for a given ice history and site by choosing the Earth structure that minimizes χ^2_{ies}:

$$\chi^2_{is} = \min_{\forall e}(\chi^2_{ies}) \tag{4}$$

This procedure assumes that the best fit to the data is obtained for the Earth structure and ice model that is closest to the true one. Note that different 1D Earth structures can be appropriate for different sites given the 3D nature of Earth's viscosity[76]. Because GIA calculations that consider only ice above floatation produce viscosity-dependent GMSL estimates, each χ^2_{is} has a distinct GMSL curve, $GMSL_{is}$.

For each ice model, we then take the mean of χ^2_{is} over all sites S, which results in a misfit value for each ice reconstruction:

$$\chi^2_i = (\frac{\sum_{s=1}^{S} \chi^2_{is}}{S}) \tag{5}$$

This statistic represents the overall fit of a given global ice-sheet history to the RSL database. We also compute a global mean sea level curve for each global ice-sheet history weighted by χ^2_{is} metrics:

$$GMSL_i = (\frac{\sum_{s=1}^{S} GMSL_{is} \cdot \chi^2_{is}}{S}) \tag{6}$$

The fitness score for each site, visualized in Fig. 5A, is calculated as the average of fitness scores (equation 4) weighted by the associated ice model's global fitness score (equation 5). Optimal Earth structures are computed for each site as the mean of the Earth structures identified in equation 4 weighted by the linear combination of local data-model misfit χ^2_{is} and global ice model weight w_i:

$$\chi^2_s = \frac{\chi^2_{is} + w_i}{\sum_{i=1}^{I} \chi^2_{is} + w_i} \tag{7}$$

Note that the denominator serves to normalize the final weights such that they sum to 1 and that χ^2_{is} and w_i are separately normalized to sum to one prior to combination. The combination of χ^2_{is} and w_i preferences local information while also including spatial covariation between sites. The relative performance of HOLSEA and non-HOLSEA databases is compared by assigning each observation the site-specific fitness value from Fig. 5A, then comparing the average fitness scores of standardized and un-standardized observations.

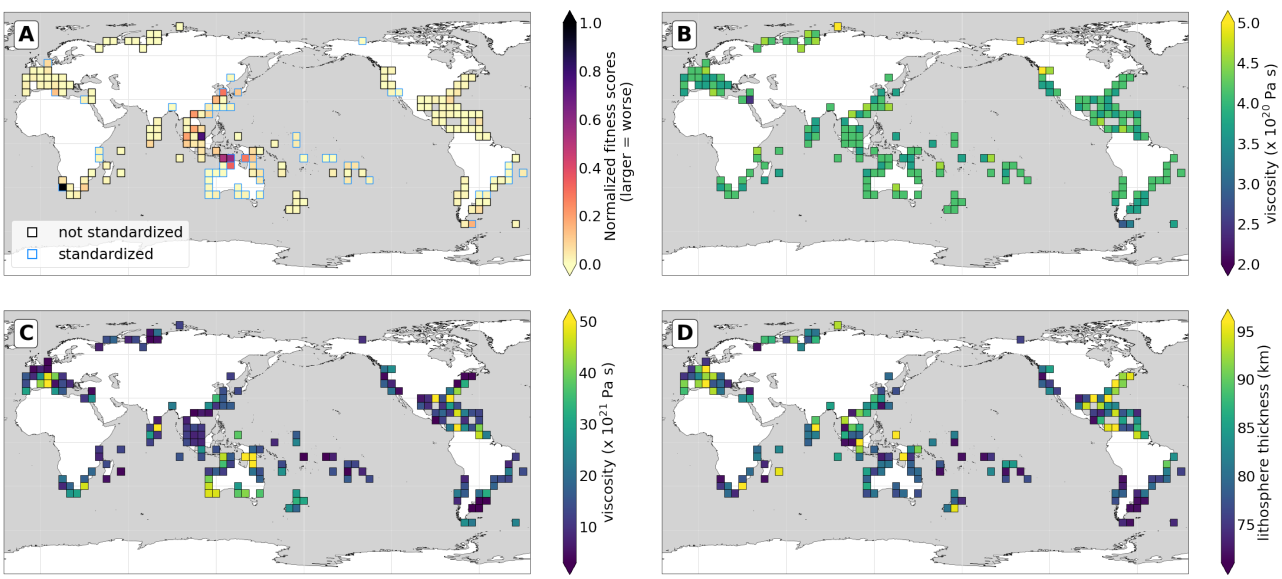

Figure 5: Fitness scores from data assimilation. **(A)** Normalized weighted mean of fitness metrics for each site. Black box indicates that the majority of RSL observations at that site are standardized; Blue box indicates not standardized. **(B)** Upper mantle viscosities. **(C)** Lower mantle viscosities. **(D)** Lithospheric thickness.

Data–model misfit and viscosity inference

Data-model misfit metrics for each sea-level data site and ice model reveal how well sites fit the ice-sheet ensemble. In contrast to most locations, misfits in the Yellow Sea, Vietnam, Timor-Leste, and Namibia are disproportionally large (Fig. 5A). A disproportionate misfit indicates that no combination of ice history and solid earth structure produced RSL curves that fit the observations at that site and accord with the full database in terms of ice history. These misfits suggest the influence of local processes such as tectonics (e.g. Timor), deltaic subsidence (e.g. Yellow Sea), or local sediment dynamics (e.g. Namibia, Cameroon). We used data from two sources: compilations following agreed-upon community standards[20;77], and published indicators not yet compiled to these standards. Standardized RSL observations are found to fit the ice-sheet ensemble 41% better than un-standardized observations (see Methods).

We find that best-fitting Earth structures are broadly coherent at both nearfield and farfield sites. Our algorithm is insensitive to upper mantle viscosity: the vast majority of sites are best fit by upper mantle viscosities around $3.5\text{x}10^{20}$ Pa s, with modestly higher viscosities near the peripheral bulges of the Laurentide and Eurasian Ice Sheets and lower viscosity in Patagonia, the US West Coast, and the Gulf of Mexico (Fig. 5B). This aligns well with the preferred global viscosity structure of[7] and the preferred upper mantle viscosity for Southeast Asia of[9], but stands in contrast to the strong upper mantle inferred by[78] for the Caribbean. Lower mantle viscosities are weakest in the intermediate field (Mediterranean, US West Coast, Caribbean) and variable in the far field. Weak lower mantle viscosities in the Caribbean accord with[78], while the bi-modal distribution of weak ($3 - 10\text{x}10^{21}$ Pa s) and strong ($\sim 5\text{x}10^{22}$ Pa s) lower mantle viscosities that we infer for Southeast Asia and Australia, respectively, accords with[7], which relies heavily on data from that region. Lithospheric thickness varies regionally from high values (>90 km) around Maine, Central Europe, and Indonesia to low values (<75 km) for Argentina, the Eastern Mediterranean, South Africa, the UK, Western Russia, US West Coast, and southern India (Fig. 5D). These patterns accord remarkably well with maps of lateral variation in lithospheric thickness[79], which also place thick lithosphere in China and in Indonesia and weak lithosphere in Western Russia, and around the UK.

That our viscosity inferences broadly accord with viscosities inferred by prior GIA-based GMSL studies increases confidence in the viability of our new method for inferring GMSL. However, we caution against over-interpretation of these viscosity maps and others based strictly on GIA models that do not include lateral variations in mantle viscosity and rely on Maxwell Earth structures. RSL is sensitive to Earth structure both locally and beneath areas of ice mass change and the degree of depth-sensitivity varies between near- and far-field sites[80]. Additionally, apparent viscosity structure as sensed by RSL data depends on the timescale of deformation, which implies that sites with predominantly older (e.g. early-mid Holocene) RSL data may sense a different viscosity structure than sites where younger (e.g. Common Era) data dominate[76;81;82]. Future efforts to invert RSL observations for viscosity structure should apply more nuanced tools such as adjoint sensitivity kernels[80].

Separate from our analysis, goodness-of-fit information for 256 of the PISM Antarctic Ice Sheet simulations used in this study was calculated by Albrecht et al.[17;21]. These fitness metrics assess how well the PISM runs align with six types of present-day observational constraints and three types of paleo-constraints. Present-day constraints include grounded area, ice shelf area, ice thickness, grounding-line location, uplift rates, and grounded surface ice speed; paleo-constraints include grounding line position at LGM as well as surface elevation and ice extent between LGM and present[17]. We perform identical fitness assessments for the additional 23 PISM Antarctic simulations published in[22], all of which include an Antarctic Ice Sheet smaller than present during the Holocene. These fitness metrics P_i are assigned to each ice ensemble member based on which PISM Antarctic reconstruction it includes.

For our prior GMSL distribution, we choose that GMSL at 6 ka is uniform between -10 and +2 meters. These values are a conservative bracket around the range of values (-3.5 to +0.5 m) chosen by the IPCC AR6 assessment report[2]. To create this uniform prior at 6 ka, we calculate a weighting factor U_i for each ice-sheet model (Extended figure 2A-C).

Putting it all together, each ice-sheet ensemble member i has a global mean sea level curve, $GMSL_i$; an associated weighting factor U_i, which produces a uniform prior at 6 ka; and a data assimilation factor (sum of fitness scores derived from RSL observations, χ_i^2, and PISM model weights, P_i), which captures how well this ice-sheet history fits non-RSL observations. Note that for the data assimilation factor we choose to sum the two scores rather than multiplying them because summation allows an overall good score to be obtained from a good fit either to sea-level observations or to ice constraints, but does not require both. This approach, which is more conservative than requiring that modeled RSL fit both observational datasets well, produces our final ice model weights w_i:

$$w_i = \frac{(\chi_i^2 + P_i) * U_i}{\sum_{i=1}^{I} (\chi_i^2 + P_i) * U_i} \tag{8}$$

Note that the denominator serves to normalize the final weights such that they sum to 1 and that U_i, χ_i^2, and P_i are separately normalized to sum to one prior to combination. The weights are multiplied with the $GMSL_i$ curve of each ice-sheet ensemble member to produce a posterior GMSL distribution. Results of this study are reported as having a ‘credible’ interval because models have an associated likelihood; uncertainty estimates from studies not produced via Bayesian methods or without associated likelihoods are reported as having a 'confidence' interval.

Synthetic tests to demonstrate model performance

Synthetic tests are performed to assess the skill of the data assimilation algorithm in estimating GMSL. We select a subset of ice histories (n=9) that represent the full range of Holocene GMSL scenarios and remove them from the ice-sheet ensemble. Spatiotemporal RSL fields are calculated from each ice history using a lithospheric thickness of 71 km, an upper mantle viscosity of 2 x 10^{20} Pa s, and a lower mantle viscosity of 40 x 10^{20} Pa s. All other GIA ensemble members with this viscosity structure are also removed from the ensemble. In addition to these 1D GIA realizations, we also include one RSL field produced by GIA calculations using laterally-varying viscosity structure, the details of which are described by Austermann and colleagues[83].

Each of the 9 1D and 1 3D RSL fields are sampled at the locations and ages of the 10,588 RSL observations and assigned uncertainties identical to those of the data. This procedure produces 10 synthetic RSL datasets. We infer a posterior GMSL using each of these synthetic datasets and the approach described in the previous section, modified such that only weights derived from RSL sources are used. We then compare the resulting GMSL to the GMSL curve associated with the ice history that produced the synthetic data. For each time step, 'coverage' is calculated as the percentage of estimated GMSL curves whose credible interval intersects the 'true' GMSL curve; the coverage test is passed if this percentage approximates the credible interval, e.g. if around 95% of comparisons pass for a 95% credible interval. Coverage for 1D and 3D simulations is shown in Fig. 4D-F for differing credible intervals. Synthetic tests with a 95% and 90% credible interval have 100% coverage between 11.5 and 6 ka and 75-90% coverage in the late Holocene; the failing models are generally those whose GMSL is higher than 1 m above present through the mid-late Holocene. Assuming a 66% credible interval yields 60% coverage or greater for all the Holocene, with failure concentrated around late Holocene high and low GMSL scenarios. That the model is able to reproduce all but the most extreme GMSL scenarios for both 1D and 3D simulations increases confidence in the application of our algorithm to estimate Holocene GMSL.

Comparison to future sea level

The IPCC Sixth Assessment Report projects that processes that can be modeled with medium confidence will contribute 0.44 m (0.32-0.61 m, at least 66% probable range) to GMSL in a low emissions scenario (SSP1-2.6) and 0.68 m (0.55-0.90 m) in a higher emissions scenario (SSP3-7.0). Concerning the Antarctic Ice Sheet, the

IPCC projects that processes that can be modeled with medium confidence will contribute 0.11 m (0.03 to 0.27 m, at least 66% probable range) to GMSL under SSP1-2.6 and 0.11 m (0.03 to 0.31 m) under SSP3-7.0. Projections for a low-likelihood, high-impact future scenario incorporating processes about which there is low confidence (SSP5-8.5) place 83rd percentile GMSL projections at 1.61 m and the 83rd percentile Antarctic contribution at 0.56 m.[2]. These values are relative to a 1995-2014 baseline period, while our GIA calculations are relative to early industrial (1850) values. We extend the IPCC baseline to 1850 with historical GMSL and Antarctic ice volume estimates from the IPCC AR6 (1950 to 2020, 1980 to 2020) and (ref.[44], 1850 to 1950; ref.[45]). Because no pre-1980 historical estimates for Antarctic ice volume exist, ref.[45] adopted a linear Antarctic contribution of 0.05$\pm$0.04 m between 1900 and 1980, which we extend to 1850.

This produces an estimate of 0.61 m (0.50-0.79 m) of GMSL rise and 0.13 m (0.05 to 0.29 m) of Antarctic Ice Sheet contribution between 1850 and 2100 for SSP1-2.6, 0.85 m (0.72-1.07 m) and 0.13 m (0.05 to 0.33 m) for SSP3-7.0, and 1.05 m (median) to 1.78 m (83rd percentile) (GMSL) and 0.21 (median) to 0.58 (83rd percentile) for SSP5-8.5 (Fig. 4). We calculate the probability that these future sea level and ice volume projections exceed our Holocene GMSL and Antarctic ice volume reconstructions by computing the fraction of the 20,000 posterior samples from each of the seven IPCC AR6 GMSL workflows[84] that exceed samples drawn from our Holocene reconstructions. Each IPCC workflow consists of a set of sea-level components—e.g. the sea level contribution of thermosteric effects or the Antarctic Ice Sheet—that were combined in order to create a probabilistic estimate of GMSL[84]. A probability envelope is produced following the IPCC-AR6 'p-box' framework[85]. For each emission scenario, the highest and lowest exceedance probabilities at each time step are chosen; this envelope represents the uncertainty in the exceedance probability estimate (Fig. S1). Only the lowest(highest) exceedance probabilities are shown for the low-probability SSP1.9 (8.5, low confidence) pathways, as these pathways represent outer boundaries on the likely amount of future sea-level rise.

Data availability

The data produced in this article can be found in supplementary material. Model outputs will be published online at zenodo.com after acceptance.

Code availability

Code to produce GIA models is available at https://github.com/jaustermann/SLcode/. Scripts for processing GIA outputs and producing plots are available on request.

Declarations of interest

The authors declare no conflicts of interest.

Acknowledgements

This work was supported by National Science Foundation grants EAR-2002352 (RC, JA) and OCE-2002437 (REK, EA). T.A. was supported by the Deutsche Forschungsgemeinschaft (DFG) in the framework of the priority program "Antarctic Research with comparative investigations in Arctic ice areas" by grants WI4556/2-1 and in the framework of the PalMod project (FKZ: 01LP1925D), supported by the German Federal Ministry of Education and Research (BMBF) as a Research for Sustainability initiative (FONA). Thanks to Matteo Vacchi, Sarah Shackleton, Christopher Piecuch, and Darrell Kaufman for their helpful correspondence, and Erica Ashe for her input throughout the project.

Author Contributions

RC, JA, and RK conceived and designed the research; RC wrote and executed the GMSL algorithm with guidance from JA and RK; JA wrote the GIA code; RC and NK compiled the data; TA supplied Antarctic Ice Sheet simulations; RC drafted figures and wrote the original draft with help from JA and RK; all authors contributed to manuscript review and editing.

References

[1] Dutton, A. *et al.* Sea-level rise due to polar ice-sheet mass loss during past warm periods. *Science* **349**, aaa4019 (2015).

[2] Fox-Kemper, B. *et al.* 2021: Ocean, cryosphere and sea level change. *The Sixth Assessment Report of the Intergovernmental Panel on Climate Change.* (2021).

[3] Kaufman, D. S. & Broadman, E. Revisiting the Holocene global temperature conundrum. *Nature* (2022).

[4] Young, N. E. *et al.* Deglaciation of the Greenland and Laurentide ice sheets interrupted by glacier advance during abrupt coolings. *Quaternary Science Reviews* **229**, 106091 (2020).

[5] Kingslake, J. *et al.* Extensive retreat and re-advance of the West Antarctic Ice Sheet during the Holocene. *Nature* **558**, 430 (2018).

[6] King, M. A., Watson, C. S. & White, D. GPS rates of vertical bedrock motion suggest late Holocene ice-sheet readvance in a critical sector of East Antarctica. *Geophysical Research Letters* **n/a**, e2021GL097232 (2022).

[7] Lambeck, K., Rouby, H., Purcell, A., Sun, Y. & Sambridge, M. Sea level and global ice volumes from the Last Glacial Maximum to the Holocene. *Proceedings of the National Academy of Sciences* **111**, 15296–15303 (2014).

[8] Peltier, W. R., Argus, D. F. & Drummond, R. Space geodesy constrains ice age terminal deglaciation: The global ICE-6G_C (VM5a) model. *Journal of Geophysical Research: Solid Earth* **120**, 450–487 (2015).

[9] Bradley, S. L., Milne, G. A., Horton, B. P. & Zong, Y. Modelling sea level data from China and Malay-Thailand to estimate Holocene ice-volume equivalent sea level change. *Quaternary Science Reviews* **137**, 54–68 (2016).

[10] Kaufman, D. *et al.* Holocene global mean surface temperature, a multi-method reconstruction approach. *Scientific Data* **7**, 201 (2020).

[11] Cuffey, K. M. *et al.* Deglacial temperature history of West Antarctica. *Proceedings of the National Academy of Sciences* **113**, 14249–14254 (2016).

[12] Farrell, W. E. & Clark, J. A. On Postglacial Sea Level. *Geophysical Journal of the Royal Astronomical Society* **46**, 647–667 (1976).

[13] Gowan, E. J. Global ice sheet reconstruction for the past 80000 years (2019).

[14] Siegert, M. J. *et al.* Major Ice Sheet Change in the Weddell Sea Sector of West Antarctica Over the Last 5,000 Years. *Reviews of Geophysics* **57**, 1197–1223 (2019).

[15] Johnson, J. S. *et al.* Review article: Existing and potential evidence for Holocene grounding line retreat and readvance in Antarctica. *The Cryosphere* **16**, 1543–1562 (2022).

[16] Jones, R. S. *et al.* Stability of the Antarctic Ice Sheet during the pre-industrial Holocene. *Nature Reviews Earth & Environment* **3**, 500–515 (2022).

[17] Albrecht, T., Winkelmann, R. & Levermann, A. Glacial-cycle simulations of the Antarctic Ice Sheet with the Parallel Ice Sheet Model (PISM) – Part 2: Parameter ensemble analysis. *The Cryosphere* **14**, 633–656 (2020).

[18] Pittard, M., Whitehouse, P. L., Bentley, M. & Small, D. An ensemble of Antarctic deglacial simulations constrained by geological observations. *Quaternary Science Reviews* (2022).

[19] Yousefi, M., Milne, G. A. & Latychev, K. Glacial isostatic adjustment of the Pacific Coast of North America: The influence of lateral Earth structure. *Geophysical Journal International* **226**, 91–113 (2021).

[20] Khan, N. S. *et al.* Inception of a global atlas of sea levels since the Last Glacial Maximum. *Quaternary Science Reviews* **220**, 359–371 (2019).

[21] Albrecht, T., Winkelmann, R. & Levermann, A. Glacial-cycle simulations of the Antarctic Ice Sheet with the Parallel Ice Sheet Model (PISM) – Part 1: Boundary conditions and climatic forcing. *The Cryosphere* **14**, 599–632 (2020).

[22] Albrecht, T. PISM glacial cycle sensitivity experiments of the Antarctic Ice Sheet (2019).

[23] Briner, J. P. *et al.* Rate of mass loss from the Greenland Ice Sheet will exceed Holocene values this century. *Nature* **586**, 70–74 (2020).

[24] Dalton, A. S. *et al.* An updated radiocarbon-based ice margin chronology for the last deglaciation of the North American Ice Sheet Complex. *Quaternary Science Reviews* **234**, 106223 (2020).

[25] Erb, M. P. *et al.* Reconstructing Holocene temperatures in time and space using paleoclimate data assimilation. *EGUsphere* 1–48 (2022).

[26] Osman, M. B. *et al.* Globally resolved surface temperatures since the Last Glacial Maximum. *Nature* **599**, 239–244 (2021).

[27] Neuhaus, S. U. *et al.* Did Holocene climate changes drive West Antarctic grounding line retreat and re-advance? 30 (2020).

[28] Briner, J. P. *et al.* Holocene climate change in Arctic Canada and Greenland. *Quaternary Science Reviews* **147**, 340–364 (2016).

[29] Matsuoka, K. *et al.* Antarctic ice rises and rumples: Their properties and significance for ice-sheet dynamics and evolution. *Earth-Science Reviews* **150**, 724–745 (2015).

[30] Ingólfsson, Ó. *et al.* Antarctic glacial history since the Last Glacial Maximum: An overview of the record on land. *Antarctic Science* **10**, 326–344 (1998).

[31] Grant, K. M. *et al.* Rapid coupling between ice volume and polar temperature over the past 150,000 years. *Nature* **491**, 744–747 (2012).

[32] Tigchelaar, M., Timmermann, A., Pollard, D., Friedrich, T. & Heinemann, M. Local insolation changes enhance Antarctic interglacials: Insights from an 800,000-year ice sheet simulation with transient climate forcing. *Earth and Planetary Science Letters* **495**, 69–78 (2018).

[33] Bova, S., Rosenthal, Y., Liu, Z., Godad, S. P. & Yan, M. Seasonal origin of the thermal maxima at the Holocene and the last interglacial. *Nature* **589**, 548–553 (2021).

[34] Marcott, S. A., Shakun, J. D., Clark, P. U. & Mix, A. C. A Reconstruction of Regional and Global Temperature for the Past 11,300 Years. *Science* **339**, 1198–1201 (2013).

[35] Solomina, O. N. *et al.* Holocene glacier fluctuations. *Quaternary Science Reviews* **111**, 9–34 (2015).

[36] Zhou, Y. & McManus, J. Extensive evidence for a last interglacial Laurentide outburst (LILO) event. *Geology* (2022).

[37] Fischer, H. *et al.* Palaeoclimate constraints on the impact of 2 °C anthropogenic warming and beyond. *Nature Geoscience* **11**, 474–485 (2018).

[38] Clark, P. U. *et al.* Sea-level commitment as a gauge for climate policy. *Nature Climate Change* **8**, 653–655 (2018).

[39] Rohling, E. J. *et al.* Asynchronous Antarctic and Greenland ice-volume contributions to the last interglacial sea-level highstand. *Nature Communications* **10**, 5040 (2019).

[40] Chambers, C., Greve, R., Obase, T., Saito, F. & Abe-Ouchi, A. Mass loss of the Antarctic ice sheet until the year 3000 under a sustained late-21st-century climate. *Journal of Glaciology* 1–13 (2021).

[41] Rockström, J. *et al.* A safe operating space for humanity. *Nature* **461**, 472–475 (2009).

[42] Klein Goldewijk, K., Beusen, A., van Drecht, G. & de Vos, M. The HYDE 3.1 spatially explicit database of human-induced global land-use change over the past 12,000 years. *Global Ecology and Biogeography* **20**, 73–86 (2011).

[43] Vollset, S. E. *et al.* Fertility, mortality, migration, and population scenarios for 195 countries and territories from 2017 to 2100: A forecasting analysis for the Global Burden of Disease Study. *The Lancet* **396**, 1285–1306 (2020).

[44] Walker, J. S., Kopp, R. E., Little, C. M. & Horton, B. P. Timing of emergence of modern rates of sea-level rise by 1863. *Nature Communications* **13**, 966 (2022).

[45] Frederikse, T. *et al.* The causes of sea-level rise since 1900. *Nature* **584**, 393–397 (2020).

[46] Badgeley, J. A., Steig, E. J., Hakim, G. J. & Fudge, T. J. Greenland temperature and precipitation over the last 20,000 years using data assimilation. *Climate of the Past* **16**, 1325–1346 (2020).

[47] Shackleton, S. *et al.* Evolution of mean ocean temperature in Marine Isotope Stage 4. *Climate of the Past* **17**, 2273–2289 (2021).

[48] Gangadharan, N. *et al.* Process-based estimate of global-mean sea-level changes in the Common Era. *Earth System Dynamics* **13**, 1417–1435 (2022).

[49] Leclercq, P. W., Oerlemans, J. & Cogley, J. G. Estimating the Glacier Contribution to Sea-Level Rise for the Period 1800–2005. *Surveys in Geophysics* **32**, 519–535 (2011).

[50] Marzeion, B., Kaser, G., Maussion, F. & Champollion, N. Limited influence of climate change mitigation on short-term glacier mass loss. *Nature Climate Change* **8**, 305–308 (2018).

[51] Shennan, I., Long, A. J. & Horton, B. P. *Handbook of Sea-Level Research* (John Wiley & Sons, 2015).

[52] Heaton, T. J. *et al.* MARINE20—THE MARINE RADIOCARBON AGE CALIBRATION CURVE (0–55,000 CAL BP). *Radiocarbon* 1–42 (2020).

[53] Hogg, A. G. *et al.* SHCal20 Southern Hemisphere Calibration, 0–55,000 Years cal BP. *Radiocarbon* **62**, 759–778 (2020).

[54] Reimer, P. J. *et al.* The IntCal20 Northern Hemisphere Radiocarbon Age Calibration Curve (0–55 cal kBP). *Radiocarbon* **62**, 725–757 (2020).

[55] Gregory, J. M. *et al.* Concepts and Terminology for Sea Level: Mean, Variability and Change, Both Local and Global. *Surveys in Geophysics* **40**, 1251–1289 (2019).

[56] Mitrovica, J. X. & Milne, G. A. On post-glacial sea level: I. General theory. *Geophysical Journal International* **154**, 253–267 (2003).

[57] Kendall, R. A., Mitrovica, J. X. & Milne, G. A. On post-glacial sea level - II. Numerical formulation and comparative results on spherically symmetric models. *Geophysical Journal International* **161**, 679–706 (2005).

[58] Dziewonski, A. M. & Anderson, D. L. Preliminary reference Earth model. *Physics of the Earth and Planetary Interiors* **25**, 297–356 (1981).

[59] Lambeck, K., Purcell, A. & Zhao, S. The North American Late Wisconsin ice sheet and mantle viscosity from glacial rebound analyses. *Quaternary Science Reviews* **158**, 172–210 (2017).

[60] Lambeck, K., Purcell, A., Zhao, J. & Svensson, N.-O. The Scandinavian Ice Sheet: From MIS 4 to the end of the Last Glacial Maximum. *Boreas* **39**, 410–435 (2010).

[61] Lambeck, K., Smither, C. & Johnston, P. Sea-level change, glacial rebound and mantle viscosity for northern Europe. *Geophysical Journal International* **134**, 102–144 (1998).

[62] Tarasov, L., Dyke, A. S., Neal, R. M. & Peltier, W. R. A data-calibrated distribution of deglacial chronologies for the North American ice complex from glaciological modeling. *Earth and Planetary Science Letters* **315–316**, 30–40 (2012).

[63] Abe-Ouchi, A. *et al.* Ice-sheet configuration in the CMIP5/PMIP3 Last Glacial Maximum experiments. *Geoscientific Model Development* **8**, 3621–3637 (2015).

[64] Lecavalier, B. S. *et al.* A model of Greenland ice sheet deglaciation constrained by observations of relative sea level and ice extent. *Quaternary Science Reviews* **102**, 54–84 (2014).

[65] Buizert, C. *et al.* Greenland-Wide Seasonal Temperatures During the Last Deglaciation. *Geophysical Research Letters* **45**, 1905–1914 (2018).

[66] Waelbroeck, C. *et al.* Sea-level and deep water temperature changes derived from benthic foraminifera isotopic records. *Quaternary Science Reviews* **21**, 295–305 (2002).

[67] Malles, J.-H. & Marzeion, B. Twentieth century global glacier mass change: An ensemble-based model reconstruction. *The Cryosphere* **15**, 3135–3157 (2021).

[68] Shakun, J. D. *et al.* Regional and global forcing of glacier retreat during the last deglaciation. *Nature Communications* **6**, 8059 (2015).

[69] Raper, S. C. B. & Braithwaite, R. J. Glacier volume response time and its links to climate and topography based on a conceptual model of glacier hypsometry. *The Cryosphere* **3**, 183–194 (2009).

[70] Leclercq, P. W. & Oerlemans, J. Global and hemispheric temperature reconstruction from glacier length fluctuations. *Climate Dynamics* **38**, 1065–1079 (2012).

[71] Goelzer, H., Coulon, V., Pattyn, F., de Boer, B. & van de Wal, R. Brief communication: On calculating the sea-level contribution in marine ice-sheet models. *The Cryosphere* **14**, 833–840 (2020).

[72] Wunsch, C., Ponte, R. M. & Heimbach, P. Decadal Trends in Sea Level Patterns: 1993–2004. *Journal of Climate* **20**, 5889–5911 (2007).

[73] Gill, A. E. *Atmosphere-Ocean Dynamics* (Academic Press, 1982).

[74] Creel, R. C. *et al.* Postglacial relative sea level change in Norway. *Quaternary Science Reviews* **282**, 107422 (2022).

[75] Briggs, R. D. & Tarasov, L. How to evaluate model-derived deglaciation chronologies: A case study using Antarctica. *Quaternary Science Reviews* **63**, 109–127 (2013).

[76] Lau, H. C. P. *et al.* Inferences of Mantle Viscosity Based on Ice Age Data Sets: The Bias in Radial Viscosity Profiles Due to the Neglect of Laterally Heterogeneous Viscosity Structure. *Journal of Geophysical Research: Solid Earth* **0** (2018).

[77] Hijma, M. P. *et al.* A protocol for a geological sea-level database. In *Handbook of Sea-Level Research*, 536–553 (John Wiley & Sons, Ltd, 2015).

[78] Milne, G. A., Long, A. J. & Bassett, S. E. Modelling Holocene relative sea-level observations from the Caribbean and South America. *Quaternary Science Reviews* **24**, 1183–1202 (2005).

[79] Austermann, J. The effect of lateral variations in Earth structure on Last Interglacial sea level (2021).

[80] Crawford, O. *et al.* Quantifying the sensitivity of post-glacial sea level change to laterally varying viscosity. *Geophysical Journal International* **214**, 1324–1363 (2018).

[81] Paxman, G. J. G., Lau, H. C. P., Austermann, J., Holtzman, B. K. & Havlin, C. Inference of the Timescale-Dependent Apparent Viscosity Structure in the Upper Mantle Beneath Greenland. *AGU Advances* **4**, e2022AV000751 (2023).

[82] Simon, K. M., Riva, R. E. M. & Broerse, T. Identifying Geographical Patterns of Transient Deformation in the Geological Sea Level Record. *Journal of Geophysical Research: Solid Earth* **127**, e2021JB023693 (2022).

[83] Austermann, J., Chen, C. Y., Lau, H. C. P., Maloof, A. C. & Latychev, K. Constraints on mantle viscosity and Laurentide ice sheet evolution from pluvial paleolake shorelines in the western United States. *Earth and Planetary Science Letters* **532**, 116006 (2020).

[84] Kopp, R. E. *et al.* The Framework for Assessing Changes To Sea-level (FACTS) v1.0-rc: A platform for characterizing parametric and structural uncertainty in future global, relative, and extreme sea-level change. Preprint, Climate and Earth system modeling (2023).

[85] Cozannet, G. L., Manceau, J.-C. & Rohmer, J. Bounding probabilistic sea-level projections within the framework of the possibility theory. *Environmental Research Letters* **12**, 014012 (2017).

SUPPORTING INFORMATION FOR: "GLOBAL MEAN SEA LEVEL HIGHER THAN PRESENT DURING THE HOLOCENE"

Roger C. Creel*[1], Jacqueline Austermann[1], Nicole S. Khan[2], Robert Kopp[3], Torsten Albrecht[4], Jonathan Kingslake[1],

1. Lamont-Doherty Earth Observatory, Columbia University, New York, USA.
2. Dept of Earth Science and Swire Institute of Marine Science, University of Hong Kong, Hong Kong.
3. Department of Earth and Planetary Sciences and Rutgers Institute of Earth, Ocean, and Atmospheric Sciences, Rutgers University, New Jersey, USA.
4. Potsdam Institute for Climate Impacts Research, Germany, USA.

*rcreel@ldeo.columbia.edu

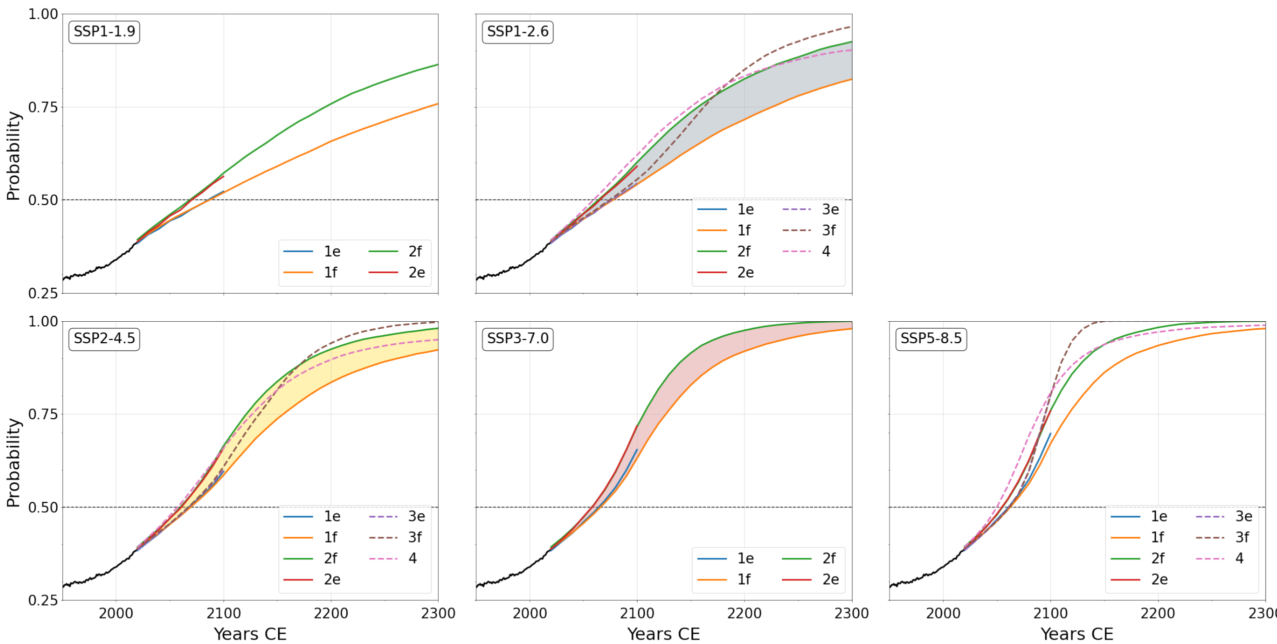

Figure S1: Exceedance probabilities for each global mean sea level (GMSL) workflow from the IPCC AR6. Colored lines denote individual IPCC AR6 workflows (i.e. 1e, 1f, 2e, 2f, 3e, 3f, 4) that incorporate processes about which there is medium (solid lines) or low (dashed line) confidence. Colored envelopes represent p-box distributions based on medium-confidence workflows. Exceedance probability describes the probability that future GMSL exceeds maximum Holocene GMSL. Workflows are described in ref. (Kopp *et al.*, 2023)

	Region	Source reference	Data #
1	Global	Hibbert *et al.* (2016)	136
2	New Zealand	Clement *et al.* (2016) and references therein	206
3	US Atlantic coast	Engelhart & Horton (2012) and references therein	813
4	US Pacific coast	Engelhart *et al.* (2015) and references therein	531
5	Northeastern Florida	Hawkes *et al.* (2016)	25
6	Russian Arctic	Baranskaya *et al.* (2018) and references therein	114
7	Southern Africa	Cooper *et al.* (2018)	59
8	Israel	Dean *et al.* (2019)	107
9	Atlantic coast of Europe	García-Artola *et al.* (2018) and references therein	319
10	Rhine-Meuse Delta	Hijma & Cohen (2019) and references therein	106
11	Southeast Asia, Maldives, India & Sri Lanka	Mann *et al.* (2019) and references therein	527
12	Malay Peninsula	Tam *et al.* (2018) and references therein	95
13	Western Mediterranean	Vacchi *et al.* (2018)	233
14	US Atlantic Coast, Newfoundland	Kemp *et al.* (2018)	785
15	Caribbean	Khan *et al.* (2017)	674
16	Florida	Khan *et al.* (2022)	410
17	US Atlantic & Gulf coasts	Love *et al.* (2016) and references therein	854
18	Southern California & Monterey Bay	Reynolds & Simms (2015) and references therein	180
19	China	Zong (2004) and references therein	235
20	North Australia	Woodroffe (2009) and references therein	81
21	Caribbean & South America	Milne *et al.* (2005)	91
22	British Isles of Scilly	Barnett *et al.* (2020)	110
23	Singapore	Chua *et al.* (2021)	20
24	North Wales, UK	Rushby *et al.* (2019)	39
25	South Georgia, sub-Antarctic	Barlow *et al.* (2016)	9
26	Chile	Garrett *et al.* (2020) and references therein	148
27	South China Sea	Xiong *et al.* (2018)	16
28	Central Pacific	Woodroffe *et al.* (2012)	107
29	Central & Western Mediterranean	Vacchi *et al.* (2021) and references therein	345
30	Global	Hibbert *et al.* (2018) and references therein	721
31	South Korea	Song *et al.* (2018) and references therein	22
32	East China	Xiong *et al.* (2020)	17
33	Australia	Dougherty *et al.* (2019)	5

Table S1: List of source references for standardized relative sea level observations.

#	Region	Source reference	Data #
34	Australia	Lewis *et al.* (2013) and references therein	350
35	Indonesia	Bender *et al.* (2020)	20
36	Central South Pacific	Hallmann *et al.* (2020)	78
37	French Polynesia	Hallmann *et al.* (2018)	98
38	Nile Delta	Marriner *et al.* (2012)	86
39	South Australia	Belperio *et al.* (2002)	212
44	Ryukyu, Japan	Yokoyama *et al.* (2016) and references therein	15
45	Philippines	Miklavič *et al.* (2018)	10
46	Iriomote Island, Japan	Yamano *et al.* (2019)	15
47	Southeast Australia	Sloss *et al.* (2007) and references therein	176
48	Western Japan	Tanigawa *et al.* (2013)	32
49	Great Barrier Reef, Australia	Leonard *et al.* (2018)	94
50	Great Barrier Reef, Australia	Salas-Saavedra *et al.* (2018)	89
51	Society Islands, Pacific	Gischler *et al.* (2016)	31
52	Brazil	Dechnik *et al.* (2019)	61
53	Río de la Plata, South America	Prieto *et al.* (2017) and references therein	56
54	Brazil	Angulo *et al.* (2018)	9
55	Malay Peninsula	Zhang *et al.* (2021)	14
56	Mekong river delta, Vietnam	Ta *et al.* (2021) and references therein	16
57	Brazil	Angulo & Lesso (1997)	39
58	Tanzania	Punwong *et al.* (2018)	16
59	Beaufort Sea	O'Regan *et al.* (2018)	8
60	Namibia	Runds *et al.* (2019)	6
61	Namibia	Kirkpatrick *et al.* (2019)	7
62	Sardinia	Deiana *et al.* (2021)	2
63	Iberian margin	Leorri *et al.* (2013)	11
64	NE Adriatic Sea	Brunović *et al.* (2020)	8
65	Tunisia	Pleuger *et al.* (2019)	30
66	Tunisia	Khadraoui *et al.* (2019) and references therein	18
67	Society Islands, Pacific	Gischler *et al.* (2019)	24
68	NE Adriatic Sea	Kaniewski *et al.* (2021) and references therein	43
69	Western Mediterranean	Vacchi *et al.* (2020)	18
70	Tierra del Fuego, Chile	Björck *et al.* (2021) and references therein	83
71	Gilbert Islands, Pacific	Yamano *et al.* (2017)	13
72	Marshall Islands, Pacific	Kench *et al.* (2014)	8
73	Cook Islands, Pacific	Gray & Hein (2005)	32
74	Rio de Janiero	Castro *et al.* (2014)	9
75	Zanzibar	Punwong *et al.* (2013); Punwong (2013)	3
76	Bonaparte Gulf, Australia	De Deckker & Yokoyama (2009)	5
77	Russian Island, Sea of Japan	Grebennikova *et al.* (2020)	1
78	Bangladesh	Rashid *et al.* (2013)	13
79	Sri Lanka	Ratnayake *et al.* (2017)	4

Table S2: List of Source references for additional published relative sea level data.

References

Angulo & Lesso, 1997. The Brazilian sea-level curves: A critical review with emphasis on the curves from the Paranaguáand Cananéia regions, *Marine Geology*, **140**(1-2), 141–166.

Angulo, R. J., de Souza, M. C., Barboza, E. G., Rosa, M. L. C. d. C., Fernandes, L. A., Guedes, C. C. F., de Oliveira, L. H. S., Manzolli, R. P., Disaró, S. T., Ferreira, A. G., & Martin, C. M., 2018. Quaternary sea-level changes and coastal evolution of the Island of Trindade, Brazil, *Journal of South American Earth Sciences*, **84**, 208–222.

Baranskaya, A. V., Khan, N. S., Romanenko, F. A., Roy, K., Peltier, W. R., & Horton, B. P., 2018. A postglacial relative sea-level database for the Russian Arctic coast, *Quaternary Science Reviews*, **199**, 188–205.

Barlow, N. L. M., Bentley, M. J., Spada, G., Evans, D. J. A., Hansom, J. D., Brader, M. D., White, D. A., Zander, A., & Berg, S., 2016. Testing models of ice cap extent, South Georgia, sub-Antarctic, *Quaternary Science Reviews*, **154**, 157–168.

Barnett, R. L., Charman, D. J., Johns, C., Ward, S. L., Bevan, A., Bradley, S. L., Camidge, K., Fyfe, R. M., Gehrels, W. R., Gehrels, M. J., Hatton, J., Khan, N. S., Marshall, P., Maezumi, S. Y., Mills, S., Mulville, J., Perez, M., Roberts, H. M., Scourse, J. D., Shepherd, F., & Stevens, T., 2020. Nonlinear landscape and cultural response to sea-level rise, *Science Advances*, **6**(45), eabb6376.

Belperio, A. P., Harvey, N., & Bourman, R. P., 2002. Spatial and temporal variability in the Holocene sea-level record of the South Australian coastline, *Sedimentary Geology*, **150**(1), 153–169.

Bender, M., Mann, T., Stocchi, P., Kneer, D., Schöne, T., Illigner, J., Jompa, J., & Rovere, A., 2020. Late Holocene (0–6 ka) sea-level changes in the Makassar Strait, Indonesia, *Climate of the Past*, **16**(4), 1187–1205.

Björck, S., Lambeck, K., Möller, P., Waldmann, N., Bennike, O., Jiang, H., Li, D., Sandgren, P., Nielsen, A. B., & Porter, C. T., 2021. Relative sea level changes and glacio-isostatic modelling in the Beagle Channel, Tierra del Fuego, Chile: Glacial and tectonic implications, *Quaternary Science Reviews*, **251**, 106657.

Brunović, D., Miko, S., Hasan, O., Papatheodorou, G., Ilijanić, N., Miserocchi, S., Correggiari, A., & Geraga, M., 2020. Late Pleistocene and Holocene paleoenvironmental reconstruction of a drowned karst isolation basin (Lošinj Channel, NE Adriatic Sea), *Palaeogeography, Palaeoclimatology, Palaeoecology*, **544**, 109587.

Castro, J. W. A., Suguio, K., Seoane, J. C., Cunha, A. M. D., & Dias, F. F., 2014. Sea-level fluctuations and coastal evolution in the state of Rio de Janeiro, southeastern Brazil, *Anais da Academia Brasileira de Ciências*, **86**(2), 671–683.

Chua, S., Switzer, A. D., Li, T., Chen, H., Christie, M., Shaw, T. A., Khan, N. S., Bird, M. I., & Horton, B. P., 2021. A new Holocene sea-level record for Singapore, *The Holocene*, p. 09596836211019096.

Clement, A. J., Whitehouse, P. L., & Sloss, C. R., 2016. An examination of spatial variability in the timing and magnitude of Holocene relative sea-level changes in the New Zealand archipelago, *Quaternary Science Reviews*, **131**, 73–101.

Cooper, J. A. G., Green, A. N., & Compton, J. S., 2018. Sea-level change in southern Africa since the Last Glacial Maximum, *Quaternary Science Reviews*, **201**, 303–318.

De Deckker, P. & Yokoyama, Y., 2009. Micropalaeontological evidence for Late Quaternary sea-level changes in Bonaparte Gulf, Australia, *Global and Planetary Change*, **66**(1), 85–92.

Dean, S., Horton, B. P., Evelpidou, N., Cahill, N., Spada, G., & Sivan, D., 2019. Can we detect centennial sea-level variations over the last three thousand years in Israeli archaeological records?, *Quaternary Science Reviews*, **210**, 125–135.

Dechnik, B., Bastos, A. C., Vieira, L. S., Webster, J. M., Fallon, S., Yokoyama, Y., Nothdurft, L., Sanborn, K., Batista, J., Moura, R., & Amado-Filho, G., 2019. Holocene reef growth in the tropical southwestern Atlantic: Evidence for sea level and climate instability, *Quaternary Science Reviews*, **218**, 365–377.

Deiana, G., Lecca, L., Melis, R. T., Soldati, M., Demurtas, V., & Orrù, P. E., 2021. Submarine Geomorphology of the Southwestern Sardinian Continental Shelf (Mediterranean Sea): Insights into the Last Glacial Maximum Sea-Level Changes and Related Environments, *Water*, **13**(2), 155.

Dougherty, A. J., Thomas, Z. A., Fogwill, C., Hogg, A., Palmer, J., Rainsley, E., Williams, A. N., Ulm, S., Rogers, K., Jones, B. G., & Turney, C., 2019. Redating the earliest evidence of the mid-Holocene relative sea-level highstand in Australia and implications for global sea-level rise, *PLOS ONE*, **14**(7), e0218430.

Engelhart, S. E. & Horton, B. P., 2012. Holocene sea level database for the Atlantic coast of the United States, *Quaternary Science Reviews*, **54**, 12–25.

Engelhart, S. E., Vacchi, M., Horton, B. P., Nelson, A. R., & Kopp, R. E., 2015. A sea-level database for the Pacific coast of central North America, *Quaternary Science Reviews*, **113**, 78–92.

García-Artola, A., Stéphan, P., Cearreta, A., Kopp, R. E., Khan, N. S., & Horton, B. P., 2018. Holocene sea-level database from the Atlantic coast of Europe, *Quaternary Science Reviews*, **196**, 177–192.

Garrett, E., Melnick, D., Dura, T., Cisternas, M., Ely, L. L., Wesson, R. L., Jara-Muñoz, J., & Whitehouse, P. L., 2020. Holocene relative sea-level change along the tectonically active Chilean coast, *Quaternary Science Reviews*, **236**, 106281.

Gischler, E., Hudson, J. H., Humblet, M., Braga, J. C., Eisenhauer, A., Isaack, A., Anselmetti, F. S., & Camoin, G. F., 2016. Late Quaternary barrier and fringing reef development of Bora Bora (Society Islands, south Pacific): First subsurface data from the Darwin-type barrier-reef system, *Sedimentology*, **63**(6), 1522–1549.

Gischler, E., Hudson, J. H., Humblet, M., Braga, J. C., Schmitt, D., Isaack, A., Eisenhauer, A., & Camoin, G. F., 2019. Holocene and Pleistocene fringing reef growth and the role of accommodation space and exposure to waves and currents (Bora Bora, Society Islands, French Polynesia), *Sedimentology*, **66**(1), 305–328.

Gray, S. C. & Hein, J. R., 2005. Lagoonal Reef Accretion and Holocene Sea-Level History from Three Atolls in the Cook Islands, Central South Pacific, *Journal of Coastal Research*, pp. 253–264.

Grebennikova, T., Razjigaeva, N., Ganzey, L., Ganzei, K., Arslanov, K., Maksimov, F., Petrov, A., & Kharlamov, A., 2020. Evolution of a paleolake on Russian Island (Sea of Japan) in middle-late Holocene: Record of sea-level oscillations, extreme storms and tsunami, *IOP Conference Series: Earth and Environmental Science*, **438**, 012009.

Hallmann, N., Camoin, G., Eisenhauer, A., Botella, A., Milne, G. A., Vella, C., Samankassou, E., Pothin, V., Dussouillez, P., Fleury, J., & Fietzke, J., 2018. Ice volume and climate changes from a 6000 year sea-level record in French Polynesia, *Nature Communications*, **9**(1), 285.

Hallmann, N., Camoin, G., Eisenhauer, A., Samankassou, E., Vella, C., Botella, A., Milne, G. A., Pothin, V., Dussouillez, P., Fleury, J., Fietzke, J., & Goepfert, T., 2020. Reef response to sea-level and environmental changes in the Central South Pacific over the past 6000 years, *Global and Planetary Change*, **195**, 103357.

Hawkes, A. D., Kemp, A. C., Donnelly, J. P., Horton, B. P., Peltier, W. R., Cahill, N., Hill, D. F., Ashe, E., & Alexander, C. R., 2016. Relative sea-level change in northeastern Florida (USA) during the last ∼8.0 ka, *Quaternary Science Reviews*, **142**, 90–101.

Hibbert, F. D., Rohling, E. J., Dutton, A., Williams, F. H., Chutcharavan, P. M., Zhao, C., & Tamisiea, M. E., 2016. Coral indicators of past sea-level change: A global repository of U-series dated benchmarks, *Quaternary Science Reviews*, **145**, 1–56.

Hibbert, F. D., Williams, F. H., Fallon, S. J., & Rohling, E. J., 2018. A database of biological and geomorphological sea-level markers from the Last Glacial Maximum to present, *Scientific Data*, **5**(1), 180088.

Hijma, M. P. & Cohen, K. M., 2019. Holocene sea-level database for the Rhine-Meuse Delta, The Netherlands: Implications for the pre-8.2 ka sea-level jump, *Quaternary Science Reviews*, **214**, 68–86.

Kaniewski, D., Marriner, N., Cheddadi, R., Morhange, C., Vacchi, M., Rovere, A., Faivre, S., Otto, T., Luce, F., Carre, M.-B., Benčić, G., & Van Campo, E., 2021. Coastal submersions in the north-eastern Adriatic during the last 5200 years, *Global and Planetary Change*, **204**, 103570.

Kemp, A. C., Wright, A. J., Edwards, R. J., Barnett, R. L., Brain, M. J., Kopp, R. E., Cahill, N., Horton, B. P., Charman, D. J., Hawkes, A. D., Hill, T. D., & van de Plassche, O., 2018. Relative sea-level change in Newfoundland, Canada during the past ∼3000 years, *Quaternary Science Reviews*, **201**, 89–110.

Kench, P. S., Chan, J., Owen, S. D., & McLean, R. F., 2014. The geomorphology, development and temporal dynamics of Tepuka Island, Funafuti atoll, Tuvalu, *Geomorphology*, **222**, 46–58.

Khadraoui, A., Zaïbi, C., Carbonel, P., Bonnin, J., & Kamoun, F., 2019. Ostracods and mollusks in northern Sfax coast: Reconstruction of Holocene paleoenvironmental changes and associated forcing, *Geo-Marine Letters*, **39**.

Khan, N. S., Ashe, E., Horton, B. P., Dutton, A., Kopp, R. E., Brocard, G., Engelhart, S. E., Hill, D. F., Peltier, W. R., Vane, C. H., & Scatena, F. N., 2017. Drivers of Holocene sea-level change in the Caribbean, *Quaternary Science Reviews*, **155**, 13–36.

Khan, N. S., Ashe, E., Moyer, R. P., Kemp, A. C., Engelhart, S. E., Brain, M. J., Toth, L. T., Chappel, A., Christie, M., Kopp, R. E., & Horton, B. P., 2022. Relative sea-level change in South Florida during the past ~5 years, *Global and Planetary Change*, p. 103902.

Kirkpatrick, L. H., Green, A. N., & Pether, J., 2019. The seismic stratigraphy of the inner shelf of southern Namibia: The development of an unusual nearshore shelf stratigraphy, *Marine Geology*, **408**, 18–35.

Kopp, R. E., Garner, G. G., Hermans, T. H. J., Jha, S., Kumar, P., Slangen, A. B. A., Turilli, M., Edwards, T. L., Gregory, J. M., Koubbe, G., Levermann, A., Merzky, A., Nowicki, S., Palmer, M. D., & Smith, C., 2023. The Framework for Assessing Changes To Sea-level (FACTS) v1.0-rc: A platform for characterizing parametric and structural uncertainty in future global, relative, and extreme sea-level change, Preprint, Climate and Earth system modeling.

Leonard, N. D., Welsh, K. J., Clark, T. R., x. Feng, Y., Pandolfi, J. M., & x. Zhao, J., 2018. New evidence for "far-field" Holocene sea level oscillations and links to global climate records, *Earth and Planetary Science Letters*, **487**, 67–73.

Leorri, E., Fatela, F., Drago, T., Bradley, S. L., Moreno, J., & Cearreta, A., 2013. Lateglacial and Holocene coastal evolution in the Minho estuary (N Portugal): Implications for understanding sea-level changes in Atlantic Iberia, *The Holocene*, **23**(3), 353–363.

Lewis, S. E., Sloss, C. R., Murray-Wallace, C. V., Woodroffe, C. D., & Smithers, S. G., 2013. Post-glacial sea-level changes around the Australian margin: A review, p. 74.

Love, R., Milne, G. A., Tarasov, L., Engelhart, S. E., Hijma, M. P., Latychev, K., Horton, B. P., & Törnqvist, T. E., 2016. The contribution of glacial isostatic adjustment to projections of sea-level change along the Atlantic and Gulf coasts of North America, *Earth's Future*, **4**(10), 440–464.

Mann, T., Bender, M., Lorscheid, T., Stocchi, P., Vacchi, M., Switzer, A. D., & Rovere, A., 2019. Holocene sea levels in Southeast Asia, Maldives, India and Sri Lanka: The SEAMIS database, *Quaternary Science Reviews*, **219**, 112–125.

Marriner, N., Flaux, C., Morhange, C., & Kaniewski, D., 2012. Nile Delta's sinking past: Quantifiable links with Holocene compaction and climate-driven changes in sediment supply?, *Geology*, **40**(12), 1083–1086.

Miklavič, B., Yokoyama, Y., Urata, K., Miyairi, Y., & Kan, H., 2018. Holocene relative sea level history from phreatic overgrowths on speleothems (POS) on Minami Daito Island, Northern Philippine Sea, *Quaternary International*, **471**, 359–368.

Milne, G. A., Long, A. J., & Bassett, S. E., 2005. Modelling Holocene relative sea-level observations from the Caribbean and South America, *Quaternary Science Reviews*, **24**(10), 1183–1202.

O'Regan, M., Coxall, H., Hill, P., Hilton, R., Muschitiello, F., & Swärd, H., 2018. Early Holocene sea level in the Canadian Beaufort Sea constrained by radiocarbon dates from a deep borehole in the Mackenzie Trough, Arctic Canada, *Boreas*, **47**(4), 1102–1117.

Pleuger, E., Goiran, J. P., Mazzini, I., Delile, H., Abichou, A., Gadhoum, A., Djerbi, H., Piotrowska, N., Wilson, A., Fentress, E., Ben Jerbania, I., & Fagel, N., 2019. Palaeogeographical and palaeoenvironmental reconstruction of the Medjerda delta (Tunisia) during the Holocene, *Quaternary Science Reviews*, **220**, 263–278.

Prieto, A. R., Mourelle, D., Peltier, W. R., Drummond, R., Vilanova, I., & Ricci, L., 2017. Relative sea-level changes during the Holocene in the Río de la Plata, Argentina and Uruguay: A review, *Quaternary International*, **442**, 35–49.

Punwong, P., 2013. *Holocene Mangrove Dynamics and Sea Level Changes: Records from the Tanzanian Coast*, Ph.D. thesis, University of York.

Punwong, P., Marchant, R., & Selby, K., 2013. Holocene mangrove dynamics from Unguja Ukuu, Zanzibar, *Quaternary International*, **298**, 4–19.

Punwong, P., Selby, K., & Marchant, R., 2018. Holocene mangrove dynamics and relative sea-level changes along the Tanzanian coast, East Africa, *Estuarine, Coastal and Shelf Science*, **212**, 105–117.

Rashid, T., Suzuki, S., Sato, H., Monsur, M., & Saha, S., 2013. Relative sea-level changes during the Holocene in Bangladesh, *Journal of Asian Earth Sciences*, **64**, 136–150.

Ratnayake, A. S., Sampei, Y., Ratnayake, N. P., & Roser, B. P., 2017. Middle to late Holocene environmental changes in the depositional system of the tropical brackish Bolgoda Lake, coastal southwest Sri Lanka, *Palaeogeography, Palaeoclimatology, Palaeoecology*, **465**, 122–137.

Reynolds, L. C. & Simms, A. R., 2015. Late Quaternary relative sea level in Southern California and Monterey Bay, *Quaternary Science Reviews*, **126**, 57–66.

Runds, M. J., Bordy, E. M., & Pether, J., 2019. Late Quaternary sedimentological history of a submerged gravel barrier beach complex, southern Namibia, *Geo-Marine Letters*, **39**(6), 469–491.

Rushby, G. T., Richards, G. T., Gehrels, W. R., Anderson, W. P., Bateman, M. D., & Blake, W. H., 2019. Testing the mid-Holocene relative sea-level highstand hypothesis in North Wales, UK, *The Holocene*, **29**(9), 1491–1502.

Salas-Saavedra, M., Dechnik, B., Webb, G. E., Webster, J. M., Zhao, J.-x., Nothdurft, L. D., Clark, T. R., Graham, T., & Duce, S., 2018. Holocene reef growth over irregular Pleistocene karst confirms major influence of hydrodynamic factors on Holocene reef development, *Quaternary Science Reviews*, **180**, 157–176.

Sloss, C. R., Murray-Wallace, C. V., & Jones, B. G., 2007. Holocene sea-level change on the southeast coast of Australia: A review, *The Holocene*, **17**(7), 999–1014.

Song, B., Yi, S., Yu, S.-Y., Nahm, W.-H., Lee, J.-Y., Lim, J., Kim, J., Yang, Z., Han, M., Jo, K.-N., & Saito, Y., 2018. Holocene relative sea-level changes inferred from multiple proxies on the west coast of South Korea, *Palaeogeography, Palaeoclimatology, Palaeoecology*, **496**.

Ta, T. K. O., Nguyen, V. L., Saito, Y., Gugliotta, M., Tamura, T., Nguyen, T. M. L., Truong, M. H., & Bui, T. L., 2021. Latest Pleistocene to Holocene stratigraphic record and evolution of the Paleo-Mekong incised valley, Vietnam, *Marine Geology*, **433**, 106406.

Tam, C.-Y., Zong, Y., bin Hassan, K., bin Ismal, H., binti Jamil, H., Xiong, H., Wu, P., Sun, Y., Huang, G., & Zheng, Z., 2018. A below-the-present late Holocene relative sea level and the glacial isostatic adjustment during the Holocene in the Malay Peninsula, *Quaternary Science Reviews*, **201**, 206–222.

Tanigawa, K., Hyodo, M., & Sato, H., 2013. Holocene relative sea-level change and rate of sea-level rise from coastal deposits in the Toyooka Basin, western Japan, *The Holocene*, **23**(7), 1039–1051.

Vacchi, M., Ghilardi, M., Melis, R. T., Spada, G., Giaime, M., Marriner, N., Lorscheid, T., Morhange, C., Burjachs, F., & Rovere, A., 2018. New relative sea-level insights into the isostatic history of the Western Mediterranean, *Quaternary Science Reviews*, **201**, 396–408.

Vacchi, M., Ghilardi, M., Stocchi, P., Furlani, S., Rossi, V., Buosi, C., Rovere, A., & De Muro, S., 2020. Driving mechanisms of Holocene coastal evolution in the Bonifacio Strait (Western Mediterranean), *Marine Geology*, **427**, 106265.

Vacchi, M., Joyse, K. M., Kopp, R. E., Marriner, N., Kaniewski, D., & Rovere, A., 2021. Climate pacing of millennial sea-level change variability in the central and western Mediterranean, *Nature Communications*, **12**(1), 4013.

Woodroffe, C. D., McGregor, H. V., Lambeck, K., Smithers, S. G., & Fink, D., 2012. Mid-Pacific microatolls record sea-level stability over the past 5000 yr, *Geology*, **40**(10), 951–954.

Woodroffe, S. A., 2009. Testing models of mid to late Holocene sea-level change, North Queensland, Australia, *Quaternary Science Reviews*, **28**(23), 2474–2488.

Xiong, H., Zong, Y., Qian, P., Huang, G., & Fu, S., 2018. Holocene sea-level history of the northern coast of South China Sea, *Quaternary Science Reviews*, **194**, 12–26.

Xiong, H., Zong, Y., Li, T., Long, T., Huang, G., & Fu, S., 2020. Coastal GIA processes revealed by the early to middle Holocene sea-level history of east China, *Quaternary Science Reviews*, **233**, 106249.

Yamano, H., Kayanne, H., Yamaguchi, T., Inoue, T., Mochida, Y., & Baba, S., 2017. Revisiting late Holocene sea-level change from the Gilbert Islands, Kiribati, west-central Pacific Ocean, *Quaternary Research*, **88**(3), 400–408.

Yamano, H., Inoue, T., Adachi, H., Tsukaya, K., Adachi, R., & Baba, S., 2019. Holocene sea-level change and evolution of a mixed coral reef and mangrove system at Iriomote Island, southwest Japan, *Estuarine, Coastal and Shelf Science*, **220**, 166–175.

Yokoyama, Y., Maeda, Y., Okuno, J., Miyairi, Y., & Kosuge, T., 2016. Holocene Antarctic melting and lithospheric uplift history of the southern Okinawa trough inferred from mid- to late-Holocene sea level in Iriomote Island, Ryukyu, Japan, *Quaternary International*, **397**, 342–348.

Zhang, Y., Zong, Y., Xiong, H., Li, T., Fu, S., Huang, G., & Zheng, Z., 2021. The middle-to-late Holocene relative sea-level history, highstand and levering effect on the east coast of Malay Peninsula, *Global and Planetary Change*, **196**, 103369.

Zong, Y., 2004. Mid-Holocene sea-level highstand along the Southeast Coast of China, *Quaternary International*, **117**(1), 55–67.